ELSEVIER

Contents lists available at ScienceDirect

International Journal of Fatigue

journal homepage: www.elsevier.com/locate/ijfatigue





A framework to enable microstructure-sensitive location-specific fatigue life analysis of components and connectivity to the product lifecycle

Saikiran Gopalakrishnan, Ritwik Bandyopadhyay, Michael D. Sangid *

Purdue University, School of Aeronautics and Astronautics, USA

ARTICLE INFO

Keywords:
Component lifing
Location specific
Microstructure sensitive
Digital twin
dual microstructure heat treated (DMHT)
Crystal plasticity

ABSTRACT

Traditionally, aerospace components are treated as monolithic structures during lifing analyses, wherein distinct microstructural information at individual locations is not necessarily considered. In components with gradient microstructures, the resulting material allowables are conservative and associated with large uncertainty bounds. To improve precision in the life estimates, a location-specific lifing framework is developed, which tracks manufacturing processes and retrieves microstructural information at distinct locations for use within a crystal plasticity fatigue life prediction model. A use case for the lifing of a dual microstructure heat treated turbine disk component is demonstrated near the bore (fine grains) and rim (coarse grains) regions. We employ the framework to access (a) the grain size statistics and (b) the macroscopic strain fields to inform precise boundary conditions for the crystal plasticity analysis. The proposed location-specific lifing framework presents new opportunities for simultaneously designing the component and tailoring the microstructures to meet the targeted performance.

1. Introduction

The performance of a component and its underlying material is governed by process-structure-property relationships [1]. The manufacturing process controls the underlying microstructure in the material, which in turn governs the mechanical properties and the ultimate performance. Hence, by controlling the processing conditions, we could potentially tailor the material's microstructure to meet the targeted performance requirements and develop next-generation components. A dual-microstructure heat treated (DMHT) turbine disk [2-4] is an example of a component produced with distinct microstructures at individual locations to meet the desired location-specific performance requirements. To maximize fatigue resistance in the bore region of the Ni-based superalloy disk, fine grain microstructures are produced by exposing the bore region to a sub-solvus (below the γ' solvus temperature) heat treatment process. On the other hand, for achieving improved resistance to creep and dwell fatigue at higher temperatures, coarse grain microstructures are produced in the rim region of the disk via a super-solvus heat treatment. For such gradient microstructures, new methodologies are needed for location-specific lifing approaches. In this work, we present a holistic framework, including capturing the design and manufacturing information throughout the product lifecycle, to efficiently assess the fatigue life of components with tailored and/or gradient microstructures by utilizing a microstructure-sensitive computational approach.

Traditionally, while lifing a component, the minimum allowable fatigue life in the material is identified through fatigue testing using specimens, which are representative of the component. While following this approach, the entire component is treated as a monolithic structure (i.e. assuming all the locations having similar microstructures and mechanical properties), and the fatigue test data, regardless of the origins of the excised test specimens relative to the component location, is combined for statistical analysis as a single population, often-times resulting in large uncertainty bounds [5]. The minimum allowable life to crack initiation is classically identified as either (i) the -3 standard deviations from the mean value of the material's low cycle fatigue life or (ii) the lower bound life corresponding to a probability of failure of 1/ 1000 (i.e. the B0.1 life), which could lead to overly conservative estimates [6,7]. However, to life microstructure-tailored components with gradient microstructures across the volume of the component, opportunities exist to employ a location-specific fatigue life analysis approach by treating separate datasets, corresponding to the distinct microstructures, in individual regions/locations of the component [5]. The location-specific lifing approach presents the potential to (i) reduce the

E-mail address: msangid@purdue.edu (M.D. Sangid).

 $^{^{\}ast}$ Corresponding author.

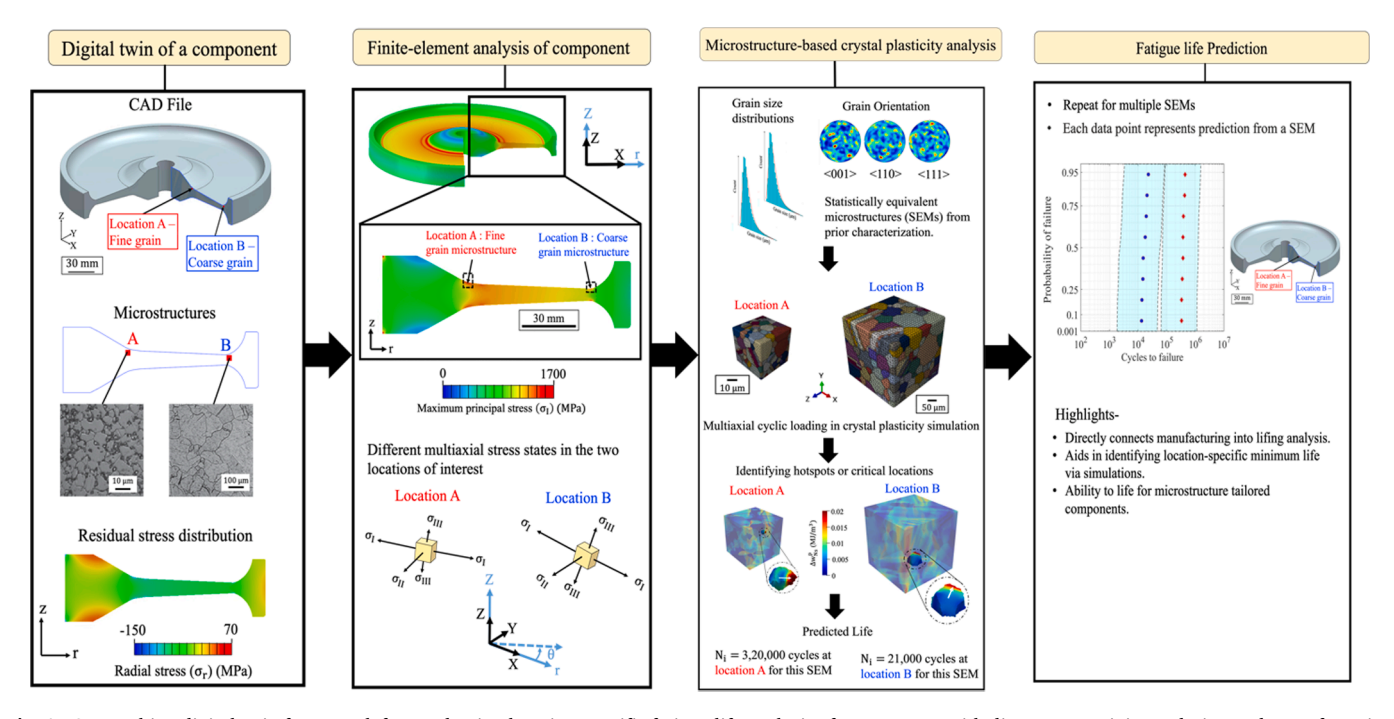


Fig. 1. Overarching digital twin framework for conducting location-specific fatigue life analysis of components with direct connectivity to design and manufacturing data workflows and in-service loading states via microstructure-sensitive crystal plasticity-based life predictions.

uncertainties in fatigue life predictions originating from the traditional lifting approach and (ii) identify life-limiting locations in the component requiring attention during inspection or additional considerations for design modifications [5,8].

Microstructure-sensitive fatigue life prediction frameworks via crystal plasticity finite-element (CPFE) simulations present opportunities to use a physics-based approach to evaluate location-specific fatigue life in a component. Within crystal plasticity [9,10], microstructural grain-level information is used and the elastic and plastic anisotropies are incorporated while evaluating distributions of strain accumulation and stresses. Energy-based fatigue indicative metrics [11–15] have been proposed to predict the fatigue crack initiation by combining the contributions of both the plastic strain (which captures dislocation motion) and shear stress (the resistance to the dislocation motion). Bandyopadhyay et al. [13] presented a single energybased fatigue metric (critical value of the accumulated plastic strain energy density or W^p_{critical} referred to as a material property), applicable for predicting fatigue crack initiation across multiple loading [13] and temperature conditions [14]. However, to effectively use this type of modeling approach for conducting location-specific fatigue life analysis of components within a workflow, the results of the manufacturing process, including precise microstructural descriptors, are required to instantiate the crystal plasticity models. In this work, we create connectivity between the component's geometric definitions and its location-specific microstructural information for use within the crystalplasticity analysis.

The vision of a digital twin [16,17] aligns well with our current goal, which is to create a digital replica of a serialized component, including geometric and non-geometric definitions, and use the current available knowledge to evaluate the future performance of the component. A digital twin can be created before the physical production of the component (i.e. during the design stages), and the information applicable to the component can be updated during its product lifecycle [18]. In our previous work [19], we introduced a digital twin framework for storing, tracking, and retrieving externally stored metadata applicable to either a serialized or set of components, as well as individual locations via a computer-aided design (CAD) model. In this work, we use the earlier developed location-specific data linking methods to dynamically

track and retrieve precise microstructural definitions within a component for use within crystal plasticity models, as shown in Fig. 1.

The individual locations in the component are exposed to varying stresses and strains during service, which is a function of the component geometry, applied loading conditions, and the gradient material microstructural features. These stress/strain states at distinct locations are crucial inputs to inform precise boundary and loading conditions for the sub-scale CPFE analysis. Component-scale finite-element (FE) simulations with in-service loading conditions can be used to obtain the stress/strain distributions. In our prior work [19], we developed a programmatic integration between the design definitions, manufacturing data, and stress/strain fields obtained from FE analysis tools. In this work, we extend the framework to inform loading states for sub-scale CPFE simulations (Fig. 1) by utilizing earlier developed methods to extract precise stress/strain fields from locations of interest within the component. This framework provides a new paradigm for the microstructure-sensitive, location-specific lifting of components.

The remainder of the paper is divided into the following sections. Firstly, we introduce the framework for enabling the digital twin (namely model-based feature information network or MFIN) and the location-specific data linking mechanism in Section 2. With the aim of utilizing the framework to demonstrate location-specific fatigue life analysis, we present a use-case of lifing DMHT turbine disk. The component geometry, manufacturing processing, and material's microstructural description are described in Section 3. The crystal plasticity-based fatigue life prediction framework is described in Section 4. A component-level FE analysis to simulate in-service stress/strain states is detailed in Section 5. Finally, we present the predictions of material allowable fatigue life, the location-specific fatigue life of the component, and considerations for the utilization of this overarching framework in Section 6, followed by the conclusion of the work in Section 7.

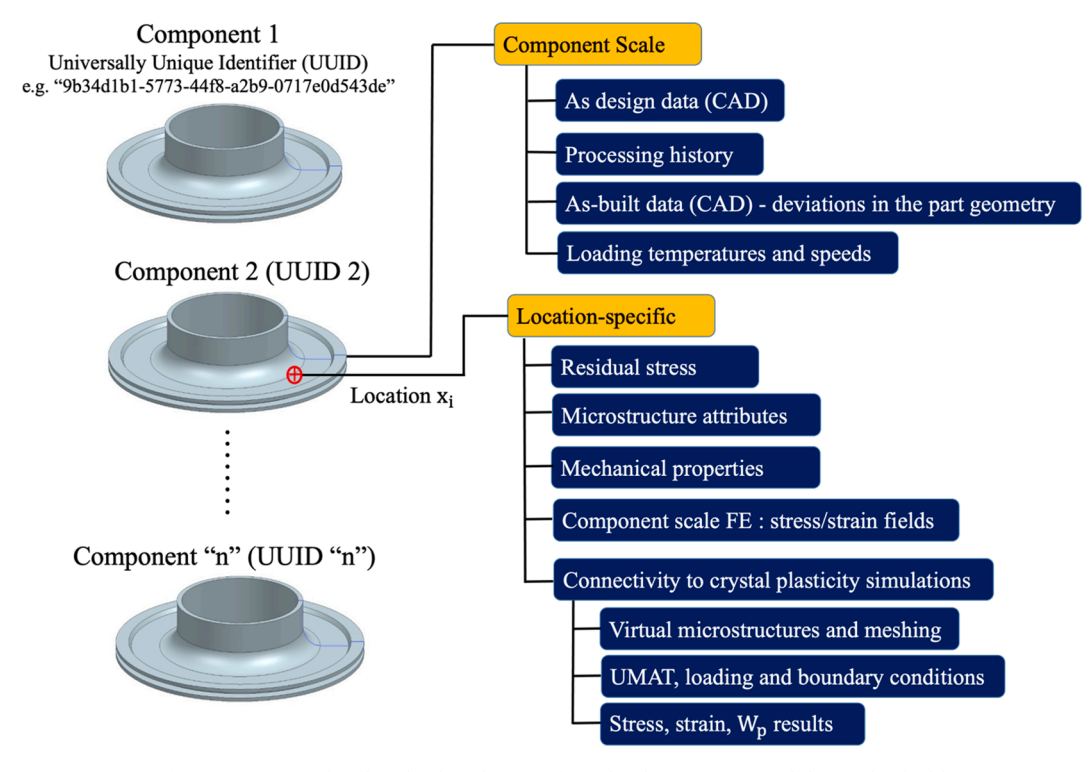


Fig. 2. Information captured within the digital twins of serialized components and their individual locations.

2. Model-based feature information network (MFIN) for creating digital twin(s) of components

2.1. File format and data linking approach

The model-based feature information network (MFIN) framework was originally developed [19,20] to integrate geometric and nongeometric data applicable to a component and its individual features, thereby facilitating the tracking and retrieval of useful information for assessing components during the product lifecycle. The MFIN framework is an extension of the Quality Information Framework (QIF) [21], which is recognized as a standard by the International Organization for Standardization for storing and communicating lifecycle metadata. The framework relies on a software-independent text file format in extensible markup language (XML), with a ".qif" file extension. This XML file format will be denoted as MFIN XML throughout the paper. The process of generating the MFIN XML file format originates from the computeraided design (CAD) model of the component. Firstly, the geometric definitions of the component and its features, along with any additional metadata in the form of notes within the CAD model, are translated into equivalent XML definitions using a software tool, namely MBDVidia [22]. In this work, we have used the Siemens NX 12.0 CAD [23] tool, while the overall framework is software agnostic to translate XML derivatives from any commercial CAD tools. Once the baseline MFIN XML file is generated from the CAD model, additional datasets from external databases or network drives are integrated, through a dynamic linking mechanism [19], with the component and its geometric features within the MFIN XML.

For capturing product lifecycle datasets other than the data originating from CAD models, we have defined new data elements within the MFIN XML. The organization of data entries within each element in the MFIN XML file is defined using the MFIN XML schema documents (XSDs) [19]. Primarily, there are two groups of MFIN schemas, namely the library schemas and the application schemas. The library schemas describe the organization of the data elements for describing the product's geometry, topology, and features. The application schemas define the layout of the data elements to capture the product lifecycle datasets

applicable either to the component level or feature level (including specific locations). In our prior work [19], we created new application schemas to define data linkages to externally stored (i) material datasets and (ii) datasets pertinent to finite-element (FE) analysis of the component. In this work, we expand the schemas to include information relevant to sub-scale crystal plasticity finite element (CPFE) analysis for connectivity to specific locations within the component. All the data elements (including geometric and non-geometric datasets), generated by following the MFIN schemas, are concatenated within the main element in the MFIN XML, namely the "QIFDocument" (dictated by the "OIFDocument.xsd" schema file).

Programmatic methods have been created for appending new data elements within the MFIN XML and retrieving existing datasets out of MFIN XML through application program interfaces (APIs) or MFIN APIs [19]. Corresponding to every data element within the MFIN schemas, Python API functions have been generated using a source code binding process [24], and all the API functions are grouped within a Python module ("QIFDocument.py"). In this work, we have used the MFIN APIs to create wrapper code(s) for linking and retrieving processing history, material microstructure descriptors, material properties, component-level FE analysis datasets, and information relevant to crystal plasticity finite element analysis (explained in Section 2.2).

The framework has been developed to dynamically store, track, update, and retrieve information at both the component-level as well as individual locations (i.e., capturing location-specific information), which has been achieved by the data linking mechanism. As opposed to storing metadata directly within the MFIN XML, the framework relies on capturing data linkages to externally stored datasets (either in the database(s) or network drives) [19]. Hence, the externally stored metadata can be continually updated, and the data linkages can be used to dynamically retrieve the most recent version of the dataset. Additionally, each data element within MFIN XML can be tracked using a unique identifier. The overall MFIN XML document is tracked using a universally unique identifier (UUID), composed of a 128-bit number following the RFC 4122 standard [25]. The UUID enables tracking of the MFIN XML corresponding to each serialized component (Fig. 2). The subelements within the MFIN XML have local identifiers, which aid in

classifying and tracking individual features. To define specific locations within the component's volume, datum points are used. Each datum point (also referred to as a point feature) is described using its location coordinate and acts as a pointer to a location within the component (Fig. 2). Following the structure of the MFIN XML, these datum points also have an associated local identifier. Hence, for creating associations between the component's geometry and metadata, the unique identifiers are grouped together with the data linkages (either file paths or database-specific identifiers [19]). The use of data linkages and the dynamic data retrieval via the MFIN framework is crucial in the context of the digital twin to continually update and utilize precise material state information tied to the component for analysis across the design, manufacturing, and service stages in the product lifecycle. The MFIN framework [19] has been integrated with several commercial materials databases, including Ansys GRANTA [26] and MSC MaterialCenter [27], wherein the material pedigree information and material datasets were housed and linked to individual features within the MFIN XML instance of a component.

As shown in Fig. 2, we can use the MFIN framework to integrate information at both the component and location-specific levels. At the component level, we can capture the as-designed geometric definitions of the component and its features (from nominal CAD model), processing history, loading conditions during service, and deviations in the part geometry post-manufacturing (from as-built CAD models) [19,28]. At the location-specific level, schemas are developed to integrate microstructural attributes, mechanical properties, stress/strain fields from component-scale FE analysis, and information pertinent to sub-scale CPFE analysis. The data linkages to retrieve microstructural definitions from individual locations are used within the CPFE analysis. Additionally, wrapper code(s) are developed to retrieve stress/strain fields from component level FE analysis and hierarchically inform boundary conditions within the CPFE simulations (explained in Section 2.2).

2.2. Hierarchical exchange of information from component-level FE analysis to sub-scale CPFE analysis

Previously [19], we created an integration between the MFIN XML and a FE analysis tool for (i) utilizing up-to-date model geometry and material properties, as well as (ii) mapping the FE analysis results (stress/strain fields) to individual locations in the design definition of the component. This was accomplished by developing a schema file, namely "MFINAnalysis.xsd" [19], to categorically store the data linkages of the input and output data. The data elements in the MFIN XML, relevant to FE analysis, include linkages to the model geometry using a STEP AP214 [29] file format, the analysis input files (".inp" files), and the analysis output files (".odb" files). Note that we utilize an intermediate STEP file derived from the native CAD model to exchange model geometry from MFIN XML to the analysis tool since the analysis tool (ABAQUS) is incompatible with directly importing XML geometric definitions [19]. Due to the dynamic updating and tracking capabilities within the MFIN XML, the geometry of the component used for the FE analysis is not limited to nominal geometries. The deviations encountered in the geometric features of the component from manufacturing or in-service incidents can be recorded and tracked via the MFIN, and a revised CAD model (and the associated STEP file) can be used to inform the updated component geometry within the analysis tool [28]. Additionally, an analysis results file (in a ".csv" file format), comprising the coordinates of elemental centroids and associated field variables (e.g., stresses, strains) of interest, can be programmatically generated and linked within the MFIN XML. Hence, corresponding to the elemental centroids in the FE analysis, point features are created within the component's geometric description within the MFIN XML, thereby mapping the analysis results to individual locations within the component. In this work, we use the MFIN framework to inform material properties for component-level FE analysis (to simulate in-service conditions) and

subsequently integrate the stresses and strains from FE analysis with the component volume.

The MFIN framework was expanded to extract strain fields from the component-level FE analysis for locations of interest to use as the boundary conditions in sub-scale CPFE analysis. For this purpose, firstly, we expanded the MFIN framework to integrate information pertinent to the CPFE analysis at distinct locations (shown in Fig. 2). Hence, we have created a new MFIN application schema ("MFINCPFEAnalysis.xsd"). The "MFINCPFEAnalysis" element within the MFIN XML is linked to specific locations via point features (using their corresponding local identifier). The sub-elements within the "MFINCPFEAnalysis" element have provisions to capture linkages to (i) the virtual discretized (fully meshed) microstructure (in ".inp" file format), (ii) grain-level information (i.e., files with grain identifiers, including grain orientations or Type II residual stresses), (iii) user-defined material sub-routine or UMAT file (".f" file format) applicable for the CPFE analysis, (iv) boundary conditions to be enforced for the CPFE simulation, and (v) the resulting micromechanical field variables extracted from the CPFE analysis. A programmatic process has been developed to inform location-specific boundary conditions within the CPFE analysis. Based on the location of interest (given by its position coordinates) within the component, the wrapper code extracts stresses/strain fields from the "MFINAnalysis" element and updates the sub-element capturing the corresponding CPFE boundary condition within the "MFINCPFEAnalysis" element. Hence, the MFIN framework enables a hierarchical exchange of location-specific FE analysis results for conducting location-specific CPFE analysis, which has been demonstrated for fatigue life assessment of a DMHT turbine disk component.

3. Dual-microstructure heat treated (DMHT) disk: Component, material and methods

To demonstrate location-specific fatigue life analysis of microstructure tailored components via the MFIN framework, we present a use case for lifing a dual microstructure heat treated turbine disk. In this section, firstly, the manufacturing process of the disk and characterization conducted in [2] are summarized. Next, the CAD model (and corresponding MFIN XML instance) of the component and the microstructure definitions across the disk are established. Finally, we create virtual microstructures for conducting location-specific CPFE analysis.

3.1. Processing route and material characterization

The DMHT disk was manufactured via a powder metallurgy processing route followed by a specialized heat-treatment process [2,3,30,31] to produce fine grains in and surrounding the bore regions of the disk and coarse grains in and surrounding the rim regions. The disk component used for the present study was developed by NASA, and the production of the disk was conducted at PCC Wyman-Gordon Forgings (initial forging and machining) and Ladish Company Inc. (specialized heat treatment) [2,3]. Initially, the LSHR powder of particle sizes less than 55 μm was hot compacted and extruded into billets. The billets were isothermally forged, followed by machining, to obtain the disk with an outer diameter of approximately 30 cm, a maximum bore thickness of 5 cm, and a maximum rim thickness of 3.8 cm [2,3]. An initial sub-solvus heat treatment was conducted at 1135 °C for 2 h, followed by air cooling to produce uniform grains across the disk with sizes ranging between $5-10 \mu m$ [2,3]. Next, the dual microstructure heat treatment was performed, wherein a temperature gradient was maintained between the bore and the rim region by means of placing a heat sink [2,3] in the bore region. This resulted in the bore region with fine grain microstructures (5 - 10 μm) and the rim region with coarse grain microstructures (30 – 80 μ m) [2,3].

Grain size distribution and texture for LSHR at different regions of the disk were characterized using the electron backscattered diffraction (EBSD) technique by Gabb et al. [2]. The characterization was

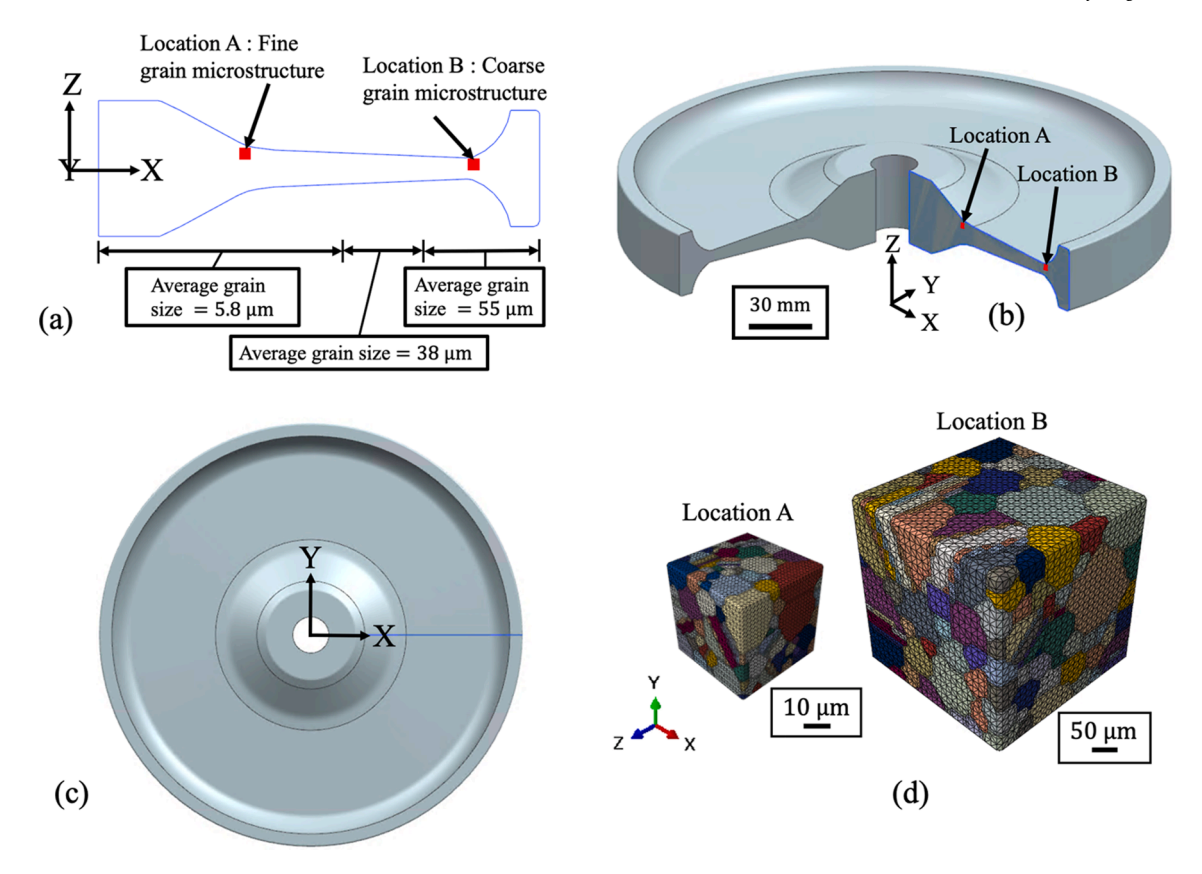


Fig. 3. Dual-microstructure heat treated (DMHT) turbine disk component: (a) 2D axisymmetric cross-section of the disk shown with average grain size information varying from fine grains (average grain size = $5.8 \mu m$) in the bore region to coarse grains (average grain size = $5.8 \mu m$) in the rim region, (b) CAD model of the disk with a 270° trimetric view, (c) top view of the entire CAD model of the disk, and (d) discretized virtual microstructures corresponding to Locations A and B.

conducted at multiple locations within the transition zone in the DMHT disk, which is a region spanning between the bore and the rim region as we move radially outward, wherein the microstructure changes from fine grains to coarse grains. The average grain size for the transition zone near the bore region was 5.8 μ m, with as-large-as (ALA) grain size of $22 \mu m$ [2]. The average grain size for the transition zone near the rim region was quantified to be 55 μ m, with ALA grain size of 413 μ m [2]. The characterized grain sizes in the near-bore region were reported to be similar to the bore region, and likewise, for the near-rim region to the exterior rim region [2]. Hence, in this work, we have consistently used an average grain size of 5.8 μm at the bore and the near-bore region and an average grain size of 55 μm across the rim and the near-rim region. The grain sizes followed lognormal distributions for both the bore and the rim region [2]. Additionally, in the central portion of the transition region, an average grain size of 38 µm was characterized, with ALA grain size of 410 μ m [2]. Throughout the disk, we have defined a random texture, based on the characterization of LSHR reported in [2,32]. Within the MFIN XML, data linkages are created between these three regions and the associate grain size attributes, which are used for the crystal plasticity-based fatigue life predictions. However, we would like to emphasize that the framework allows for defining an unlimited number of regions; hence, more refined gradient structures can be realized. Moreover, the approach can be extended to incorporate other microstructure artifacts, such as grain boundary structure, precipitate distributions, and the likelihood of pores or inclusions, obtained via characterization [4] or modeling [33].

3.2. Creation of CAD model of the turbine disk

For the geometric definition of the component, a CAD model of the DMHT turbine disk was created. We used the approximate geometric

dimensions reported in [2] and also summarized in Section 3.1 to create a 2D axisymmetric section of the disk (shown in Fig. 3(a)). The axisymmetric section was revolved about the Z-axis to generate the 3D CAD model of the DMHT disk, as shown in Fig. 3(b) and (c). The microstructural features are defined in the three regions (bore/nearbore, transition, and rim/near-rim) using semantic notes in the CAD model tagged to datum points within these regions, as shown in Fig. 3 (a). The CAD model and the associated notes were translated into the MFIN XML file using the process described in Section 2.1. For this study, we have chosen two distinct locations, Location A (fine grain microstructure) in the bore region and Location B (coarse grain microstructure) in the rim region, as shown in Fig. 3(a) and (b), respectively, with their associated microstructures - to conduct crystal plasticity-based fatigue life predictions. The locations were selected where the highest stress during service is expected (also verified later in Section 5 via component-level FE analysis) since there is a sharp change in the crosssection of the disk.

3.3. Generation of location-specific discretized virtual microstructures

We used the grain size statistics reported by Gabb et al. [2] and summarized in Section 3.1 to create 3D synthetic virtual microstructures for both Locations A and B. The detailed process for utilizing microstructure descriptors (grain size, texture, twin area fraction) and creating virtual microstructures, followed by mesh generation via a DREAM.3D pipeline, is explained in [34]. The lognormal mean and standard deviations were used to instantiate the virtual microstructures. A random texture was assigned to these microstructures. The Taylor factor was used as a measure to quantify the texture. After instantiating multiple virtual microstructures per location, statistical equivalency with respect to grain sizes, twin area fraction, and texture was verified.

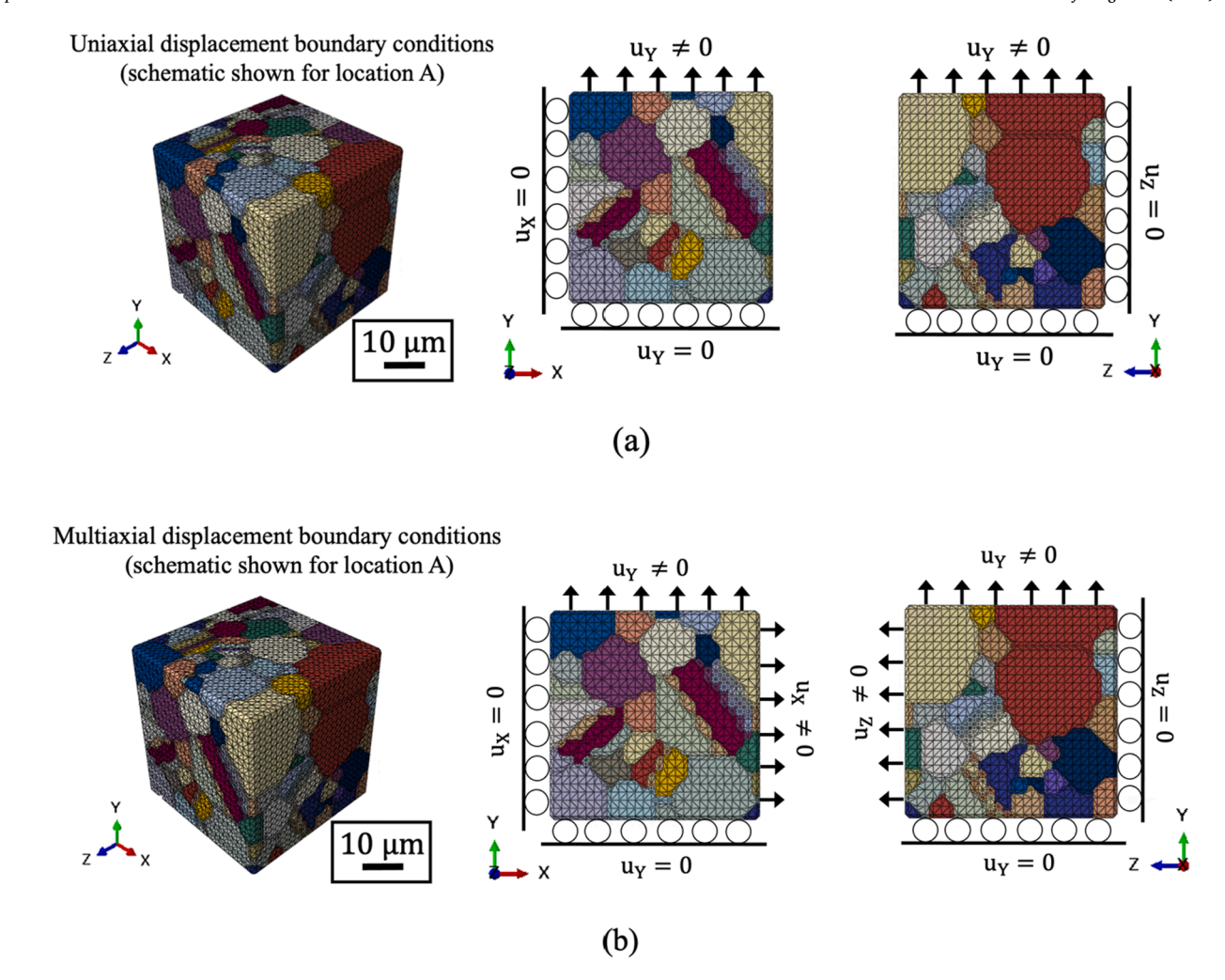


Fig. 4. Boundary conditions for the crystal plasticity finite element simulations of the discretized microstructures: (a) uniaxial displacement boundary condition to simulate experimental loading conditions and (b) multiaxial displacement boundary conditions to simulate the applied strain state at individual locations in the component.

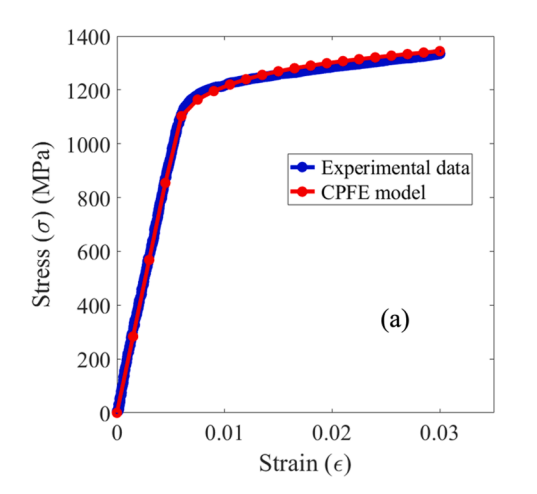
The statistical equivalency is defined based on achieving less than 5 % difference in average grain size, 5 % difference in twin area fraction, and 2 % difference in the Taylor factor [35]. For materials with random texture and high density of annealing twins, the grain misorientation distribution follows a Mackenzie distribution with an additional peak at 60° misorientation demonstrating the presence of twins; here the virtual microstructures also exhibit the same profile for the grain misorientation distribution based on the use of the twin insertion code. These virtual microstructures are referred to as statistically equivalent microstructures (SEMs). For Location A, 8 SEMs were generated with an average grain size of 5.8 μm , and the SEM domain size was 35 $\mu m \times 35$ $\mu m \times 35~\mu m.$ The grain sizes ranged from 1 μm to 24 $\mu m.$ For Location B, 8 SEMs were generated with the SEM domain size of 325 $\mu m \times$ 325 $\mu m \times$ 325 μm . The grain sizes ranged from 9 μm to 220 μm . In this study, we use an explicit approach, wherein we phenomenologically include grain size effects by choosing different SEM domain sizes corresponding to the lognormal mean and standard deviation in the grain size distributions of the microstructure, while ensuring there are sufficient number of grains included in the sampling volume to capture the macroscopic mechanical response. Each SEM consists of approximately 200 to 230 grains, as identified based on a sensitivity study for reliable fatigue life predictions in the HCF loading regime [15]. In [15], the authors have demonstrated 8-9 SEMs to capture the scatter in the fatigue life data reasonably well. Hence, for our demonstration, we have made a choice of 8 SEMs per location. Linear tetrahedral (C3D4) mesh elements were used to discretize the SEMs, and the element sizes were chosen based on a mesh sensitivity analysis conducted in [36], wherein a suitable choice of refined mesh satisfied the following criteria, $\frac{average}{average}$ $\frac{element}{size} \leq \frac{3}{48} \frac{\mu m}{\mu m} = 0.063.$ In our case, an average element size of 0.33 μm was chosen for Location A and an average element size of 2.99 μm was chosen for Location B, which is in accordance with the criteria. The SEMs were linked to individual locations in the component via MFIN XML and used for conducting CPFE simulations.

4. Crystal plasticity-based fatigue life prediction framework

Calibration of the model is necessary to conduct fatigue life predictions at two levels: (i) the crystal plasticity (CP) model parameters and (ii) the critical value of the fatigue metric, known as the critical accumulated plastic strain energy density (W^p_{critical}). In Section 4.1, we introduce the crystal plasticity model used in this work, boundary conditions for CPFE, and the model calibration. Next, we summarize the fatigue life prediction model using W^p_{critical} in Section 4.2. Finally, we present the calibration of W^p_{critical} parameter using experimental life datasets via a Bayesian inference approach in Section 4.3.

4.1. Crystal plasticity constitutive model and parameter calibration

The crystal plasticity model used in this work is based on the continuum mechanics description of slip via dislocation glide. The total



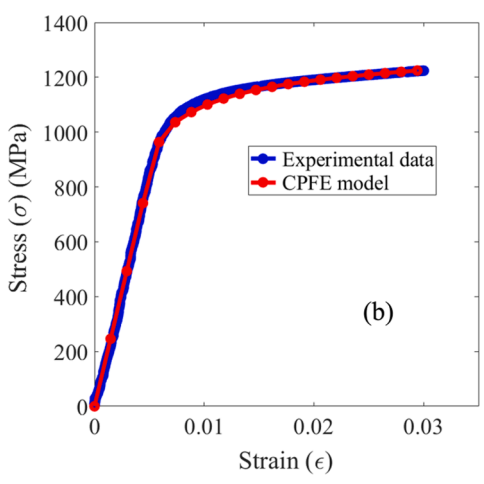


Fig. 5. Comparison of experimental and simulated macroscopic stress–strain curves from an SEM using calibrated crystal plasticity parameters for LSHR at 593 °C for (a) fine grain microstructure and (b) coarse grain microstructure.

deformation gradient (F) at a material point can be described using a multiplicative decomposition into an elastic part (F^e) (which captures the elastic stretching and rotations) and a plastic part (F^p) (which captures the plastic deformation via crystallographic slip) as shown in Eq. (1).

$$\mathbf{F} = \mathbf{F}^{\mathbf{e}} \cdot \mathbf{F}^{\mathbf{p}} \tag{1}$$

The velocity gradient (L^p) associated with the plastic part of the deformation is related to F^p using Eq. (2).

$$\mathbf{L}^{\mathbf{p}} = \dot{\mathbf{F}}^{\mathbf{p}} \cdot (\mathbf{F}^{\mathbf{p}})^{-1} \tag{2}$$

Further, L^p can be described using shear strain rate $(\dot{\gamma}^i)$, slip direction s^j and slip plane normal \mathbf{n}^j associated with the j^{th} slip system and summed over all the active slip systems using Eq. (3).

$$\mathbf{L}^{p} = \sum\nolimits_{j=1}^{12} \dot{\gamma}^{j} (\mathbf{s}^{j} \bigotimes \mathbf{n}^{j}) \tag{3}$$

The shear strain rate $(\dot{\gamma}^j)$ can be related to resolved shear stress (τ^j) on the j^{th} slip system using the Hutchinson flow rule [37] and has a power-law relationship as shown in Eq. (4).

$$\dot{\gamma}^{j} = \dot{\gamma}^{j}_{0} \left| \frac{\tau^{j}}{g^{j}} \right|^{n} sgn(\tau^{j}) \tag{4}$$

 $\dot{\gamma}_0^j$ and n are the initial shearing rate and the inverse strain rate sensitivity exponent, respectively. The reference stress (g^i) or the resistance to shearing offered by the slip system, which also evolves with plastic deformation, is described using a Taylor-type hardening law as shown in Eq. (5). g_0 is the initial slip resistance and ρ^i is the total dislocation density. The terms μ , b, and h_n represent the shear modulus, the Burgers vector, and a kinetics-based scaling parameter, respectively.

$$g^{j} = g_{0} + b\mu\sqrt{h_{n}\rho^{j}} \tag{5}$$

The evolution of ρ^j is captured via a Kocks-Mecking [38,39] relationship (Eq. (6)), which constitutes a dislocation storage term, k_1 , and a dislocation annihilation term, $k_2(\hat{\epsilon},T)$.

$$\dot{\rho}^{j} = |\dot{\gamma}^{j}| \left(k_{1} \sqrt{\rho^{j}} - k_{2}(\dot{\epsilon}, T) \rho^{j} \right) \tag{6}$$

Finally, the constants k_1 and $k_2(\dot{\epsilon},T)$ are related using Eq. (7) [40] with the temperature T and the applied strain rate $\dot{\epsilon}$. This relationship is applicable for dislocation glide mediated plasticity, wherein $10^{-5}s^{-1} \leq \dot{\epsilon} \leq 10^3 \ s^{-1}$. Here, Γ_{act} is the activation energy term, k is the Boltzmann constant, $\dot{\epsilon}_0$ is the reference strain rate, and D is a scaling constant.

$$\frac{\mathbf{k}_{2}(\dot{\boldsymbol{\varepsilon}},T)}{\mathbf{k}_{1}} = \frac{\mathbf{h}_{n}\mathbf{b}}{\Gamma_{\text{act}}} \left[1 - \frac{\mathbf{k}T}{\mathbf{D}\mathbf{b}^{3}} \ln \left(\frac{\dot{\boldsymbol{\varepsilon}}}{\dot{\boldsymbol{\varepsilon}}_{0}}\right)\right] \tag{7}$$

Hence, in the CP model, there are eleven parameters, which are to be calibrated using the experimental data. These include plasticity terms $\dot{\gamma}_0$, n, g(0), $\rho(0)$, k_1 , Γ_{act} , D, and h_n and the anisotropic elastic constants C_{11} , C_{12} , C_{44} .

Prior to calibration of the CP model parameters, we introduce two different types of boundary conditions (shown in Fig. 4) for the CPFE analyses in this study. Firstly, for calibration of the CP model parameters and critical value of the fatigue metric, we use symmetric boundary conditions for simulating the uniaxial experimental test conditions in an average sense, as shown in Fig. 4(a). The normal displacements are constrained in three mutually orthogonal faces of the SEMs, corresponding to X = 0, Y = 0, and Z = 0, respectively. A non-zero normal displacement is specified along the Y direction. The remaining two surfaces of the SEMs are unconstrained and act as free surfaces in the simulation. Next, for location-specific fatigue life predictions of the DMHT disk component, the CPFE simulations are informed hierarchically via component-level analysis and multiaxial displacement boundary conditions are applied, as shown in Fig. 4(b). Non-zero displacements are applied on three mutually orthogonal surfaces (Fig. 4 (b)) along the X, Y, and Z directions. The choice of displacements is determined via component-level FE analysis by simulating the in-service loading conditions and retrieving location-specific strain states in the component (explained in Section 5).

Linear tetrahedral (C3D4) elements are used to mesh the SEMs, which provides a conformal mesh but offers drawbacks. The values of the micromechanical field variables from the CPFE analysis are prone to spurious numerical oscillations arising from (i) volumetric locking [41], (ii) lack of mesh refinement near the grain boundaries resulting in steep gradients in field variables across grains, or (iii) poor quality of tetrahedral elements near grain boundaries and twin boundaries. To compensate for these aspects, a slip-system-based regularization scheme, namely non-local averaging, is employed [15]. At each of the integration points of the finite elements, we consider three mutually orthogonal directions corresponding to the slip direction, slip plane normal, and a transverse direction for the jth slip system, which bound a cuboidal volume about a center coinciding with the integration point. The micromechanical field variables are averaged over all the elements whose centroids lie within the bounding volume. Since we are dealing with a FCC material, we have 12 active slip systems (i.e., j = 1 to 12) and hence twelve such bounding volumes are considered for each integration point for averaging. Finally, after computing average values

Table 1 Calibrated values of CP model parameters for LSHR at 427 $^{\circ}$ C corresponding to the fine grain and coarse grain microstructures.

Parameter	Fine grain microstructure	Coarse grain microstructure
C ₁₁ (GPa)	257.9	228.0
C ₁₂ (GPa)	103.4	91.4
C44 (GPa)	77.3	68.2
$\dot{\gamma}_0$	0.0001	0.0001
n	40	40
g(0) (MPa)	460	386
$\rho(0) (1/mm^2)$	10^{6}	10^{6}
k ₁ (1/mm)	7×10^{5}	4.5×10^5
h _n	0.09	0.09
$\Gamma_{ m act}$	$2.88\mathrm{X}10^{-3}$	$2.88\mathrm{X}10^{-3}$
D (MPa)	53,280	53,280

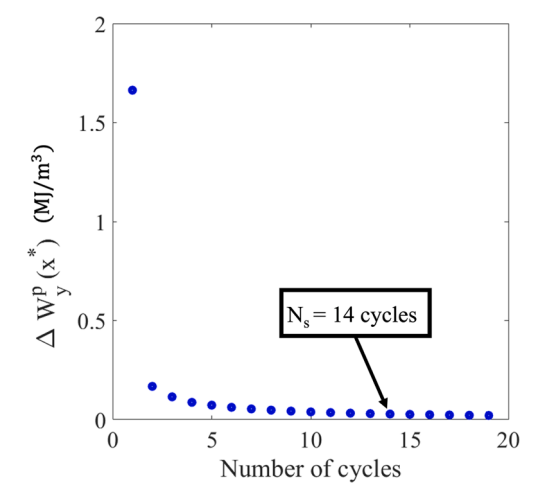


Fig. 6. Saturation of plastic strain energy density per cycle evaluated at the critical location x^* (shown for an SEM corresponding to the location with coarse grain microstructure).

corresponding to each of the twelve bounding volumes, the maximum value amongst the averages is assigned as the slip-system averaged quantity of the micromechanical variable at the integration point of interest. In our current analysis, we have used an averaging volume of 5–3–3 elements along the slip direction - plane normal - transverse direction, which was determined via a sensitivity study in [14]. The averaging volumes are truncated to ensure the non-local average is contained within a single grain, e.g., does not cross a grain boundary. Additionally, the micromechanical field values are prone to spurious values in the elements near the surfaces of the SEM wherein boundary conditions (including applied displacement constraints and tractions) are imposed. Hence, for all the CPFE analyses in this study, the micromechanical field values near the surfaces with applied boundary conditions (approximately 5-element thickness from the bounding surfaces of the SEMs) are discarded.

The fatigue analyses in this study are focused on a single isothermal temperature, 427°C, and due to the availability of data, the CP model parameters are calibrated at 593°C with appropriate scaling laws to account for temperature dependencies. For each of the fine grain and coarse grain microstructures, the CP model parameters ($\dot{\gamma}_0$, n, g(0), ρ (0), k_1 , Γ_{act} , D, and h_n) were separately calibrated using uniaxial monotonic stress–strain data (Fig. 5). The elastic constants (C₁₁, C₁₂, C₄₄) of LSHR are based on reported values in [42]. The starting point for the calibration of g(0), ρ (0), k_1 for each of the fine grain and coarse grain microstructures are based on a Kocks-Mecking approach (details included in Appendix). Additionally, the values of Γ_{act} , D, h_n , $\dot{\gamma}_0$, and n are considered independent of grain size and hence constant for both microstructures. The model parameters were iteratively adjusted until a

match between the experimental stress–strain curves and the crystal plasticity model was achieved (as shown in Fig. 5(a) and (b)). The elastic constants, C_{11} , C_{12} , C_{44} , are temperature-dependent, and hence, the values obtained at 593 $^{\circ}$ C were scaled up by 5.05 % based on [32] to obtain applicable values at 427 $^{\circ}$ C. The yield stress was reported to be insensitive between 427 $^{\circ}$ C and 593 $^{\circ}$ C; hence the values of g(0) calibrated at 593 $^{\circ}$ C were used at 427 $^{\circ}$ C. Lastly, the parameter h_n is also temperature-dependent; however, we have assumed it to be insensitive to temperature changes between 427 $^{\circ}$ C and 593 $^{\circ}$ C. The final calibrated values of the model parameters for LSHR applicable at 427 $^{\circ}$ C are summarized in Table 1, which were subsequently stored in a CSV file and linked to locations A and B in the DMHT disk via the MFIN XML.

4.2. Fatigue life prediction model using the critical value of plastic strain energy density (W_{pritical}^p)

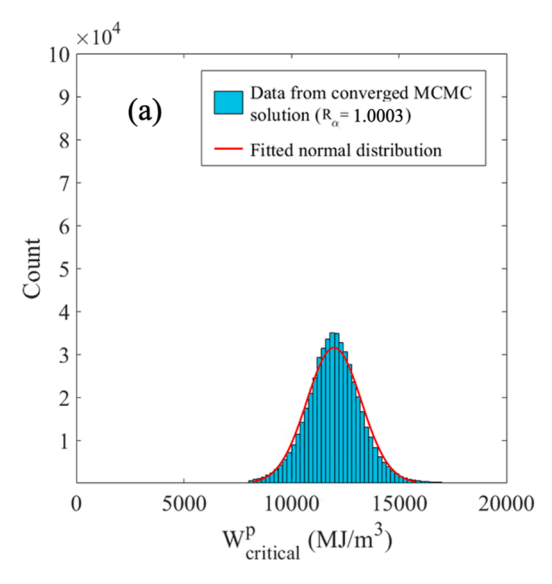
A single critical value of an energy-based fatigue metric is used to predict fatigue life. From historical origins [43], the work done by external forces during fatigue loading contributes to an elastic portion of energy (which is recoverable during unloading) and an internal plastic work (non-recoverable upon unloading). A portion of the internal plastic work is stored within the material, and this contributes to the formation of dislocation structures and sub-structures. Here at the *meso*-scale, we use the stored portion of the internal plastic work, described as the accumulated plastic strain energy density [13], for predicting fatigue life relative to microstructural features, which has been experimentally validated previously, c.f. Ref. [14,44,45]. From the CPFE analysis, the plastic strain energy density at a material point (x) within an SEM is computed by accounting for contributions from individual slip systems. For the y^{th} loading cycle, the incremental plastic strain energy density $(\Delta w_y^p(x))$ is computed using Eq. (8).

$$\Delta w_y^p(x) = \oint \Biggl(\sum\nolimits_{j=1}^{12} \left| \tau^j(x,t) \, \dot{\gamma}^j(x,t) \, \right| \, \Biggr) dt \tag{8} \label{eq:delta_w_p}$$

The accumulated plastic strain energy density, $w_y^p(x)$, over the y^{th} loading cycles is computed by summing over the accumulated cycles, $\Delta w_v^p(x)$, as shown in Eq. (9).

$$w_y^p(x) = \sum_{i=1}^y \Delta w_i^p(x) \tag{9}$$

A reduced number of cycles (Ns) is explicitly simulated, which is sufficient for the dislocation configurations in the material and the macroscopic hysteresis loop to stabilize and corresponds to a saturation in the values of $\Delta w_{\nu}^p(x)$. To identify a reasonable choice for N_s , an SEM corresponding to the coarse grain microstructure was simulated for 20 cycles. After the simulation was completed, $\Delta w_v^p(x)$ were extracted, followed by regularizing the fields via a non-local averaging scheme described in Section 4.1. Finally, we extract and plot Δw_v^p values at a critical location $x = x^*$ (Fig. 6), which corresponds to the location with the maximum accumulated plastic strain energy density value. Hence, the results from the crystal plasticity model are used to identify the location of x*, which represents the *weak link* in the microstructure prone to failure. Past work by the authors has used the location of x* to identify competing failure modes in materials [14]. The values of $\Delta w_{\nu}^{p}(x^{*})$ saturate after a few loading cycles. A similar analysis was repeated for the fine grain microstructure as well. Based on this analysis, all the CPFE simulations in the remainder of the work were performed for 14 cycles $(N_s = 14 \text{ cycles})$ and the values of $w_{N_c}^p(x^*)$ and $\Delta w_{N_c}^p(x^*)$ were extracted and used for life predictions. After N_s loading cycles, the increment in plastic strain energy density $\Delta w_v^p(x^*)$ is constant, with the values equal to Δw_N^P (x*). The extracted CPFE values associated with each SEM are linked to the corresponding location within the DMHT disk via the MFIN framework.



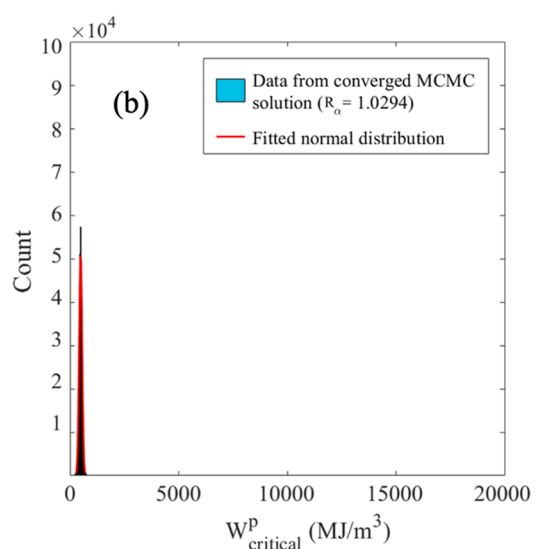


Fig. 7. Posterior distributions of accumulated plastic strain energy density (W^p_{ritical}) parameter for (a) fine grain microstructure and (b) coarse grain microstructure.

The critical value of the accumulated plastic strain energy density, W_{critical}^p , corresponding to a predicted fatigue life, N_f , is based on linear extrapolation using $\Delta w_{N_s}^p(x^*)$ from N_s to the experimentally reported fatigue life distributions (N_f^{exp}) [2] as shown in Eq. (10).

$$W_{\text{critical}}^{p} = W_{N_{c}}^{p}(x^{*}) + (N_{f}^{\text{exp}} - N_{s})\Delta W_{N_{c}}^{p}(x^{*})$$
(10)

The W_{critical}^{p} value, which is postulated to be a material property, is calibrated based on experimental results using a Bayesian inference approach.

4.3. Calibration of the accumulated plastic strain energy density $(W^{\mu}_{critical})$ using a Bayesian inference approach

There is inherent scatter associated with fatigue life, which has been attributed to variability in the microstructure features [46]. In the current framework, the statistical variability in the microstructural features is captured by creating various instantiations of virtual microstructures, SEMs. Each SEM will provide the evolution of $w_v^p(x)$ and an associated predicted lifetime to crack initiation, which can be compared to a series of results from experimental test specimens. We calibrate the value of W_{critical} using a Bayesian inference approach (please refer [13] for full details), based on matching the simulation results from a set of SEMs with the distribution of the experimentally determined cycles to failure. To calibrate W_{critical} for each of the coarse grain and fine grain microstructures, CPFE simulations were performed under uniaxial cyclic loading conditions (Fig. 4(a)). The experimental fatigue tests were conducted at an applied strain range $\Delta \varepsilon =$ 0.6 %, fatigue load ratio R =0, and at 427 °C. For each of the two types of microstructures, tests were conducted on six specimens, and the fatigue life data was reported in [2]. Hence, for calibrating W^p_{critical}, we use six fatigue life data points and eight SEMs, per microstructure.

By rearranging Eq. (10) and replacing N_f^{exp} with the predicted life $N_f^{predict}$, we can describe $N_f^{predict}$ as a function of $W_{critical}^p$, as shown in Eq. (11). This equation depicts the fatigue life prediction model used in this work. The values of $w_{N_s}^p(x^*)$ and $\Delta w_{N_s}^p(x^*)$ are obtained from CPFE simulations for each SEM, and $W_{critical}^p$ is the parameter in Eq. (11) which is to be calibrated.

$$N_f^{predict} = \frac{W_{critical}^p - w_{N_s}^p(\boldsymbol{x}^*)}{\Delta w_{N_s}^p(\boldsymbol{x}^*)} + N_s \tag{11}$$

The predicted fatigue life and experimental life can be related using

Eq. (12), wherein the term δ accounts for the errors originating from experiments and the limitations in the crystal plasticity model to capture the underlying physics. The term δ can be described using a normal distribution with zero mean and a standard deviation (s) [13]. Hence, the parameter set for the Bayesian calibration process is described as $\alpha = \{W_{\text{critical}}^p, s\}$.

$$N_f^{exp} = N_f^{predict} + \delta \tag{12}$$

The inputs required for Bayesian calibration include experimental observation (i.e., the fatigue life data) and prior distributions for $\alpha.$ The output of the Bayesian calibration process is the posterior distributions for $\alpha.$ The calibration process is separately conducted for coarse grain and fine grain microstructures. Finally, the expected values of $W^p_{critical}$ is extracted from the posterior distributions and used for fatigue life prediction.

Initially, we assume uniform prior distributions $(\pi_0(\alpha))$, which are systematically updated based on a Bayesian inference method using experimental observations (D) and likelihood function $\pi(D|\alpha)$. The posterior distribution $\pi(\alpha|D)$ can be evaluated using Bayes' theorem as shown in Eq. (13).

$$\pi(\alpha|D) = \frac{\pi(D|\alpha)\pi_0(\alpha)}{\pi(D)} = \frac{\pi(D|\alpha)\pi_0(\alpha)}{\int \pi(D|\alpha)\pi_0(\alpha)d\alpha} \tag{13} \label{eq:13}$$

The likelihood term $\pi(D|\alpha)$ in Eq. (13) can be expressed using Eq. (14) [13]. The term t is the product of the number of SEMs (n_1) times the number of experimental data points (n_2) .

$$\pi(D|\alpha) = \frac{1}{(2\pi s^2)^{\frac{1}{2}}} exp(-\frac{SSE(\alpha)}{2s^2}) \tag{14} \label{eq:14}$$

 $SSE(\alpha)$ is the sum of square errors for the parameter set α , which is described using Eq. (15). In the present work, for both the coarse grain and fine grain microstructures, we have 8 SEMs (i.e., $n_1=8$) and 6 experimentally reported [2] fatigue life data points (i.e., $n_2=6$).

$$SSE(\alpha) = \sum\nolimits_{i=1}^{n_1} \sum\nolimits_{j=1}^{n_2} \left(N_i^{exp} - N_j^{predict}(\alpha)\right)^2 \tag{15}$$

However, while evaluating the posterior distributions of α using Eq. (13), computation of the integral term in the denominator term can be challenging. To overcome this challenge, a Markov chain Monte-Carlo (MCMC) sampling approach is used. Please see [13] for the description of the MCMC approach. The posterior distributions of $W^p_{\rm critical}$, obtained using the Bayesian calibration, are presented in Fig. 7 and follow a normal distribution. These results correspond to converged MCMC

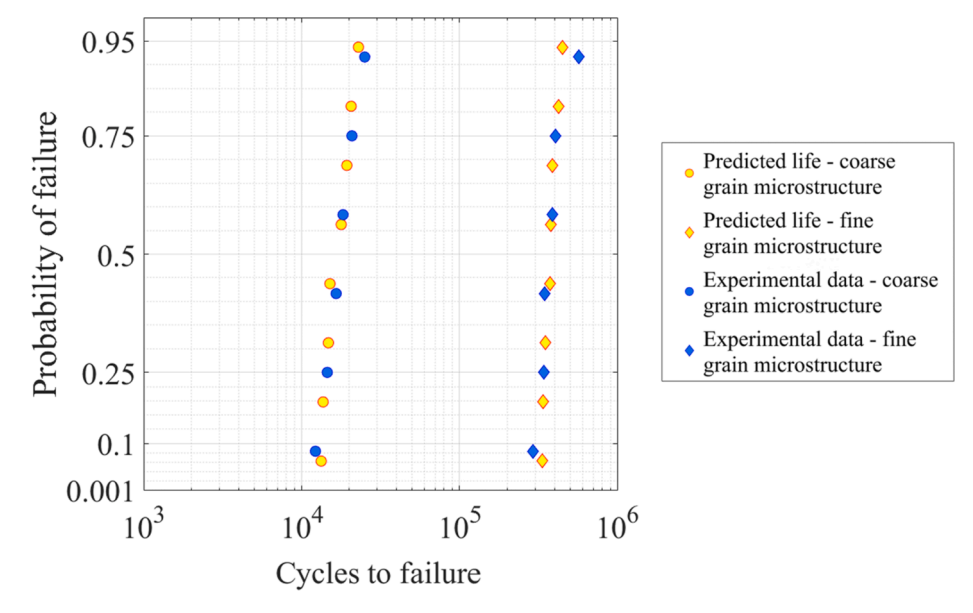


Fig. 8. Probability of failure plot comparing experimental fatigue life data (at $\Delta \varepsilon = 0.6$ %, R = 0, 427 °C) from [2] and predicted fatigue life data (each data point corresponds to an SEM) using the calibrated values of $W_{critical}^p$ for fine grain and coarse grain microstructures.

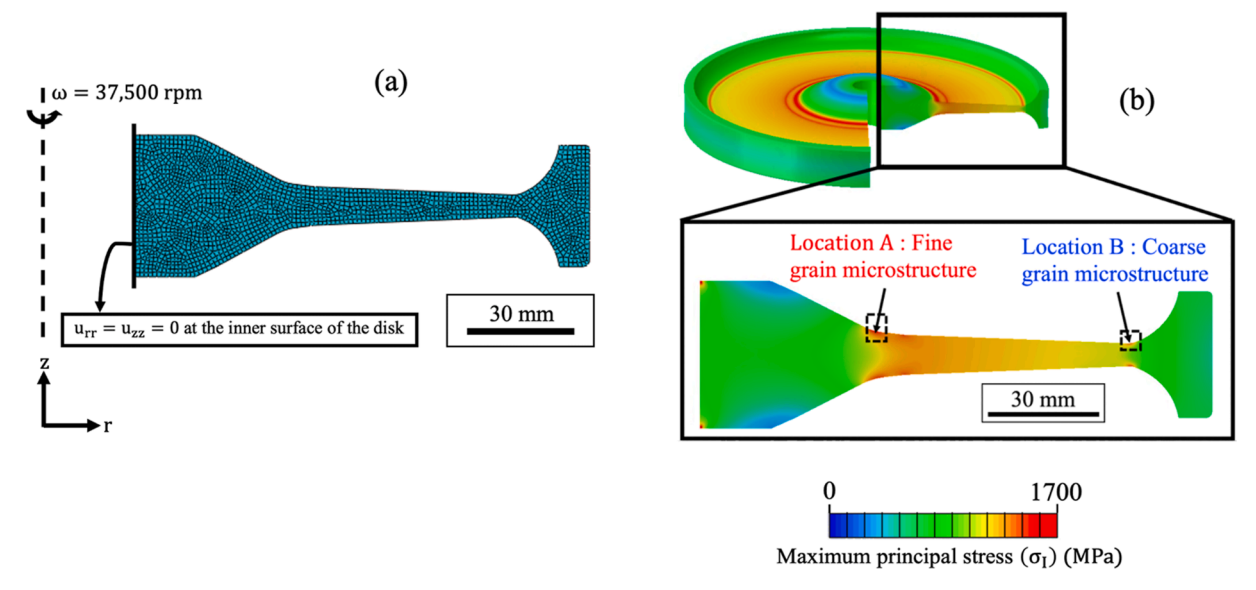


Fig. 9. Finite element model of the disk: (a) axisymmetric model geometry with quadrilateral mesh elements, centrifugal load, and boundary conditions, and (b) maximum principal stress distribution generated in the disk during service wherein the principal stresses are $\sigma_I = 1251\,\text{MPa}, \, \sigma_{II} = 774\,\text{MPa}, \, \sigma_{III} = 40\,\text{MPa}, \, \text{and}$ principal strains are $\epsilon_I = 0.0051, \, \epsilon_{II} = 0.0021, \, \epsilon_{III} = -0.0027$ at Location A and $\sigma_I = 1206\,\text{MPa}, \, \sigma_{II} = 939\,\text{MPa}, \, \sigma_{III} = 39\,\text{MPa}, \, \epsilon_{I} = 0.0053, \, \epsilon_{II} = 0.0033, \, \epsilon_{III} = -0.003$ at Location B.

solutions, wherein the value of the convergence metric R_{α} [13] was closest to 1. For the fine grain microstructure (average grain size of 5.8 μ m), we obtained mean value of $W_{critical}^{p}=11,984.8$ MJ/m³ and standard deviation of $W_{critical}^{p}=1,264.6$ MJ/m³. Whereas, for the coarse grain microstructure (average grain size of 55 μ m), we obtained the mean value of $W_{critical}^{p}=488.6$ MJ/m³ and standard deviation of $W_{critical}^{p}=69.4$ MJ/m³. The value of $W_{critical}^{p}$ is higher for the fine grain microstructure compared to the coarse grain microstructure. As discussed in [47–49], the cycles to fatigue crack initiation are higher for fine grain material compared to coarse grains, under low plastic strain amplitudes and ambient temperatures, since coarser grains are more prone to the formation of persistent slip bands (PSBs) [49,50] which leads to strain localization. The metric $W_{critical}^{p}$ is postulated as a material property, which is analogous to the energy for crack initiation via the formation of

stable dislocation structures and sub-structures, including PSBs. Hence, the observed trend in $W^p_{critical}$ with average grain size is consistent. Future work can explore the exact relationship between $W^p_{critical}$ and average grain sizes.

A probability of failure plot versus the number of cycles to failure is shown for the simulations compared to the experimental results from [2] in Fig. 8. The simulation-based predicted life and experimental datasets compare well in terms of range and slope, and both follow a lognormal distribution (see Fig. 8).

5. Component-level FE analysis

The micromechanical fields of the DMHT turbine disk were modeled for in-service conditions, from rest to an overspeed state, at an operating temperature of 427 $^{\circ}$ C. A static analysis has been performed on an

Table 2Material property values of LSHR at 427 °C which were used for the FE analysis, corresponding to the three regions (as shown in Fig. 3(a)) of the DMHT disk.

Material Properties	Bore region (Average grain size = 5.8 µm)	Transition region (Average grain size = 38 µm)	Rim region (Average grain size = 55 µm)
Density (ρ) (kg/m³)	8359	8359	8359
Young's Modulus (E) (GPa)	199.6	181.7	176.5
Poisson's ratio (ν)	0.286	0.286	0.286
Yield stress (σ_{YS}) (MPa)	1209	1112	1101
Strain hardening coefficient (B)(MPa)	3641	3078	2697
Strain hardening exponent (c1)	0.81	0.76	0.73
Temperature exponent (c2)	1	1	1
Melting temperature (T_{melt}) (°C)	1297	1297	1297

axisymmetric section of the disk to acquire stresses and strains corresponding to the maximum loading condition, while assuming the minimum applied load to be zero (therefore, the fatigue stress ratio is R=0). A centrifugal load has been applied on the disk, with a spin speed of $\omega=37500\,\mathrm{rpm}$. To enforce the constraints on the disk due to the shaft, a displacement boundary condition was applied on the inner surface of the disk in both the radial and axial directions. The analysis model with the mesh, applied loads, and boundary conditions are shown in Fig. 9(a). Linear quadrilateral elements are used with an average element size of 0.3 mm, based on a mesh sensitivity analysis.

An elastoplastic material model was used for the FE analysis following a Johnson-Cook [51] type hardening rule (Eq. (16)), wherein the flow stress ($\overline{\sigma}$) is a function of the equivalent plastic strain ($\overline{\epsilon}$) and applied temperature (T). In Eq. (20), the parameters σ_{YS} , B, c_1, c_2 , T_{ref} , T_{melt} refer to the yield stress, strain hardening coefficient, strain hardening exponent, temperature exponent, reference temperature, and melting temperature, respectively.

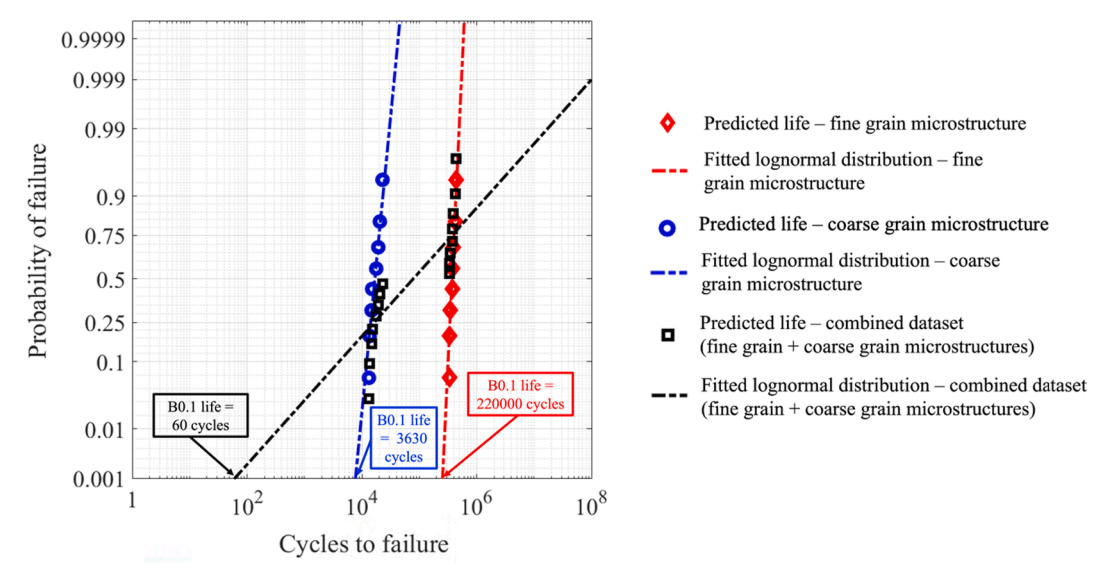


Fig. 10. Probability of failure plot versus cycles to failure with B0.1 life values obtained by treating the datasets as individual distributions per location based on the underlying microstructure (blue data points correspond to SEMs from coarse grain microstructure and red data points correspond to fine grain microstructure) compared to treating the entire dataset as one single distribution (independent of the microstructure). (For interpretation of the references to colour in this figure legend, the reader is referred to the web version of this article.)

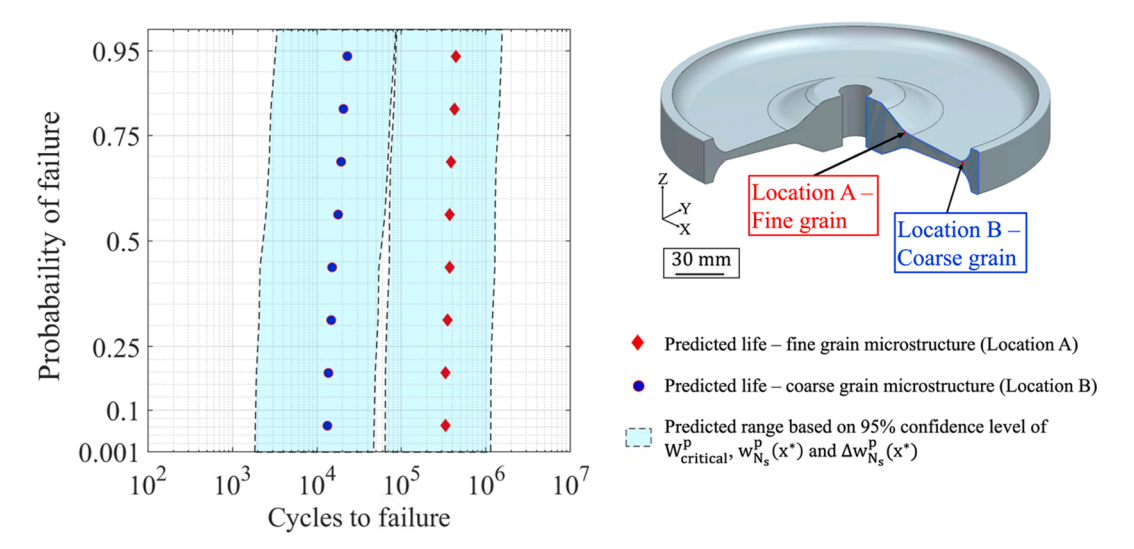


Fig. 11. Probability of failure plot corresponding to Location A (fine grain microstructure) and Location B (coarse grain microstructure) obtained via crystal plasticity simulations (each data point in the plot corresponds to an SEM).

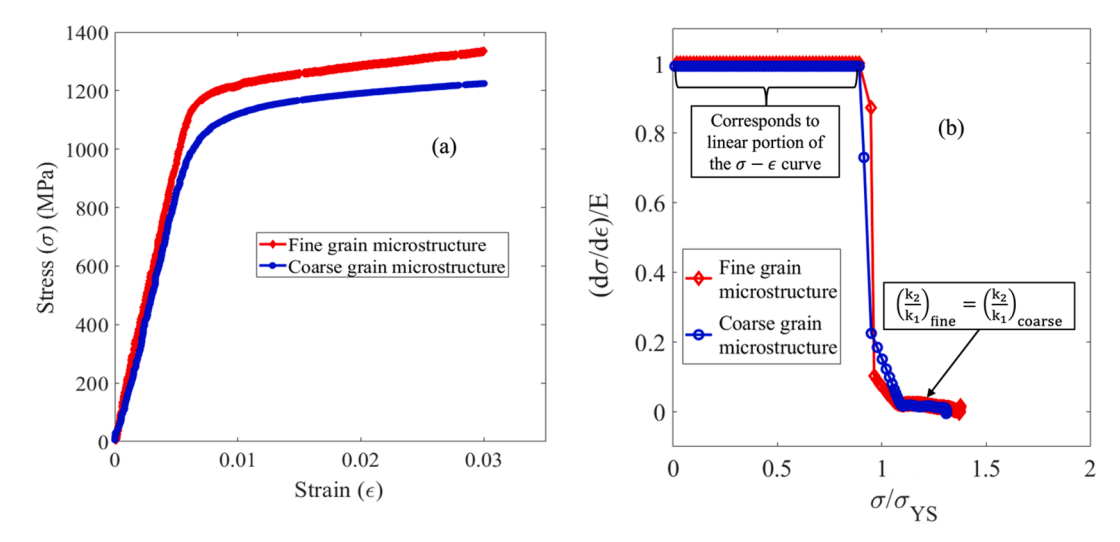


Fig. 12. Uniaxial tension test data for LSHR at 593°C corresponding to the fine grain and coarse grain microstructures: (a) stress–strain data and (b) tangent modulus $(d\sigma/d\epsilon)$ scaled by the Young's modulus (E) versus stress (σ) scaled by the yield stress (σ_{YS}) .

$$\overline{\sigma} = (\sigma_{YS} + B\overline{\epsilon}^{c_1}) \left[1 - \left(\frac{T - T_{ref}}{T_{melt} - T_{ref}} \right)^{c_2} \right]$$
 (16)

Additionally, we also use elastic model parameters, Young's modulus (E) and Poisson ratio (ν), as well as physical property, mass density (ρ) [32]. The material properties assigned to different regions (bore region, transition region, and rim region) of the disk are based on the original average grain size definitions within the MFIN XML (Fig. 3(a)). For each element in the component FE model, the average grain size is extracted from the nearest point feature (Section 3.2). The material properties of LSHR were individually calibrated for the bore region (fine grain microstructure) and the rim region (coarse grain microstructure) based on reference stress–strain data at 593 °C (Fig. 5). The material properties of LSHR corresponding to different regions of the disk are summarized in Table 2.

Using the calibrated Johnson-Cook plasticity parameters (σ_{YS} , B, and c_1) and Young's modulus (E) for the bore and rim regions, the corresponding parameters for the transition region were determined through interpolation, based on the average grain size value of 38 μ m. The physical, elastic, and plastic parameter values are stored in individual CSV files and linked to distinct regions of the DMHT disk, using the earlier created point features within the MFIN XML. Subsequently, the temperature-dependent terms in Eq. (16) were used to conduct the FE analysis for the application temperature of 427 °C.

The principal stresses and strains across the component were calculated via the FE analysis and exported within a CSV file along with the corresponding element centroid location coordinates. Thereby, point features are created within the MFIN XML of the DMHT disk, and the FE analysis results are linked to individual locations (Section 2.2). The maximum principal (σ_I) stress distribution across the disk is shown in Fig. 9(b). As expected, we observe high stresses in the region of the two locations of interest (i.e., the Locations A and B) due to the steep variation in the cross-section of the disk at these locations. Additionally, the discrete change in material properties associated with the three distinct regions of varying average grain sizes occurs at locations sufficiently far from the Locations A and B. The principal strains from Locations A and B are used to inform multiaxial displacement boundary conditions for the CPFE analysis in a hierarchical fashion via the MFIN framework. The CPFE analyses tied to Locations A and B are subsequently used for location-specific fatigue life predictions in the DMHT disk.

6. Results and discussion

The framework is used to systematically identify, store, and retrieve

site-specific material microstructure and associated properties across a component. The data is seamlessly used for (i) CPFE simulations to evaluate material allowables through uniaxial loading conditions, (ii) component level FE analysis, and (iii) hierarchical CPFE simulations with site-specific boundary conditions from the component FE analysis.

6.1. Simulation-based uniaxial minimum fatigue life for LSHR

For establishing the materials allowables by identifying the minimum fatigue life, this framework is beneficial to (i) complement experimental results with simulated predictions, thereby accounting for additional cases of extreme value statistics of microstructural features to identify the minimum life (as described in this section) and (ii) connect to component lifting analysis (Section 6.2). Here, we present the predicted fatigue life results obtained via CPFE simulations, while applying a constant uniaxial loading condition ($\Delta \varepsilon = 0.6$ %, R = 0, 427 °C) for all the SEMs (akin to fatigue testing using virtual specimens). The probability of failure versus loading cycles plot is shown in Fig. 10. In this plot, we have data points corresponding to the fine and coarse grain microstructures, representing the predicted fatigue life obtained from their respective SEMs. In addition, the lognormal fits of these datasets are included. The plot in Fig. 10 provides: (i) the predicted life corresponding to the fine grain microstructure, (ii) the predicted life corresponding to the coarse grain microstructure, and (iii) the predicted life for the combined dataset as a single distribution (i.e., similar to the traditional approach of assuming uniform microstructure across the component).

The significance of the presented result is twofold. Firstly, the use of microstructure-sensitive life predictions presents opportunities to reduce the overall number of tests needed to identify the allowable material life. Secondly, we observe reduced uncertainties in the reported fatigue life by treating datasets corresponding to individual locations as separate distributions, which was enabled by the tracking capabilities of location-specific microstructures in the MFIN framework. For identifying the minimum allowable life of the material using the B0.1 approach, we used the lognormal fits and extrapolated the value corresponding to the probability of failure of 1/1000 for each of the three cases shown in Fig. 10. The B0.1 life corresponding to the coarse grain microstructure was estimated as 3,630 cycles, whereas the B0.1 life corresponding to the fine grain microstructure was estimated as 220,000 cycles. On the other hand, while using the traditional approach of treating all the fatigue life datasets from a single loading condition as one single distribution (assuming a monolithic component), we obtain a significantly lower minimum allowable B0.1 life of 60 cycles. Hence, by

accounting for precise microstructure descriptions of the material (i.e. location-specific microstructures), while estimating the minimum allowable life of the material, we could potentially reduce uncertainties and shift our estimates to a higher minimum life. The analysis demonstrated in this work could be particularly beneficial while estimating the material allowable(s) for next-generation components with gradient microstructures.

6.2. Component level: Location-specific fatigue life predictions for the DMHT disk

Next, we describe the location-specific fatigue life predictions connected to the component (i.e., component lifing) by using pertinent location-specific loading conditions within CPFE simulations in a hierarchical fashion. As explained in Section 5, each of the SEMs, corresponding to Location A (fine grain microstructure) were simulated with multiaxial displacement boundary conditions, informed through the component scale FE analysis, by using the principal strains, $\epsilon_{\rm I}=0.0051,\,\epsilon_{\rm II}=0.0021,\,\epsilon_{\rm III}=-0.0027$ and R=0. Similarly, the SEMs corresponding to Location B (coarse grain microstructure) were simulated with $\epsilon_{\rm I}=0.0053,\,\epsilon_{\rm II}=0.0033,\,\epsilon_{\rm III}=-0.003$ and R=0, based on the component-level FE results. Here, the MFIN framework was used to track and retrieve the principal strains across the component from inservice type loading FE simulation at locations of interest and used to inform the multiaxial displacement boundary conditions for the subscale CPFE analysis (Fig. 4(b)).

The probability of failure versus loading cycles plot corresponding to Locations A (near bore) and B (near the rim) in the component is shown in Fig. 11. Each data point in the plot corresponds to the predicted life from an SEM. The predicted life for each multiaxially loaded SEM was computed using Eq. (11), wherein the corresponding $w_{N_n}^p(x^*)$ and $\Delta w_{N_s}^p(x^*)$ values were obtained from each CPFE simulation. Since $W_{critical}^p$ has been demonstrated to be applicable, independent of loading conditions [13], we used the earlier calibrated $W_{critical}^p$ values, i.e. $W_{critical}^p =$ $11984.8\,\mathrm{MJ/m^3}$ for SEMs corresponding to the fine grain microstructure (Location A) and $W^p_{critical} = 488.6\,\text{MJ}/\text{m}^3$ for SEMs corresponding to the coarse grain microstructure (Location B) in Eq. (11). In Fig. 11, a prediction range is reported to represent uncertainties corresponding to a 95 % confidence level. For calculating this prediction range, we incorporated two sources of variability [14], which include (i) the standard deviation of W^p_{critical} from the posterior distribution obtained via the Bayesian calibration process (Section 4.3) and (ii) uncertainties associated with calibration of the CP model parameters propagating to the $w_{N_{c}}^{p}(x^{*})$ values, as described in [35]. The choice of sampling volume and the number of grains in the SEMs was based on a sensitivity study, which was originally conducted under uniaxial traction boundary conditions [15]. In the current demonstration, we have assumed and used the same SEMs for CPFE simulations under both uniaxial and multiaxial loading conditions. However, separate studies would be required to determine the appropriate sampling volume of the SEMs for multiaxial loading conditions.

By identifying and tracking site-specific microstructures in the DMHT disk and conducting associated CPFE analysis via the MFIN framework, we were able to isolate fatigue life predictions connected to individual locations in the component, as shown in Fig. 11. The result shown in Fig. 11 is indicative of critical locations in the component from the context of fatigue crack initiation, thereby providing insights to the designer on when and where a crack initiates first, given the location-specific microstructural information and loading conditions. In the current demonstration, wherein we have conducted analysis at two distinct locations, it is evident that Location B (in the rim region) is prone to crack initiation at an earlier cycle count. From the context of planning the maintenance and inspection schedules during the service of the disk, the site-specific likelihood of failure is useful information. Additionally, the predictive analysis approach presents opportunities to

determine lifecycles, after which inspection and maintenance of a serialized component should be scheduled [52]. We would like to emphasize that the modeling framework used in this work focuses on fatigue life predictions for crack initiation. However, depending on the local microstructure and local geometric constraints at the site of crack initiation within the component, the crack growth rates will vary. In the near-threshold regime, coarse grain microstructures are typically more tolerant to crack growth as opposed to fine grain microstructures [53]. However, the presented MFIN framework and its location-specific tracking capabilities of local microstructure and loading states can be extended for evaluating the location-specific fatigue life via a damage tolerance analyses, including the incorporation of residual stress information [19,54].

6.3. Considerations for the microstructure-sensitive location specific life predictions

The transition towards a physics-based, microstructure-sensitive approach for lifing components, as demonstrated via the DMHT study, presents numerous advantages. By including more physics-based predictive analysis via simulating multiple SEMs, we can improve our understanding of the cause-effect relationships in the material system. We can also reduce the number of experiments needed for determining the minimum fatigue life, thereby reducing the overall costs incurred in the material qualification process. For component lifing, we presented a hierarchical approach to use the stress/strain states from the component-level FE analysis within the microstructure-sensitive CPFE analysis. The approach is computationally tractable, since it does not rely on modeling the entire component's microstructure. In this study, we have demonstrated lower length scale analysis in two locations experiencing high stress values. However, the determination of the critical locations of failure are dependent on additional factors, including stress gradients, local pre-existing damage, geometric constraints on a cracked surface, local microstructure, etc. Based on these factors, as well as legacy lifecycle records from prior versions of the component, lifing engineers can determine critical locations to perform lower length scale CPFE simulations. Moreover, the approach does not rely on homogenization; hence we can directly incorporate microstructural variability at each component location of interest by simulating multiple SEMs and therefore account for extreme values of microstructural attributes while predicting fatigue life. The CPFE analysis used in this work employed individual sets of model parameters corresponding to distinct microstructures. Further work can include strain gradient CPFE approaches [55], which can implicitly capture grain size effects via a single set of crystal plasticity model parameters applicable to multiple locations in the component. Lastly, this modeling framework can be extended to include finer discretization in the microstructure attributes across the spatial regions or include more rich microstructural information, including precipitate distribution, the likelihood of porosity/inclusions, residuals stresses, or surface effects.

The capability of the MFIN framework has been presented for storing, tracking, and updating material microstructural information tied to individual locations in the component. The use of the data linking approach within the MFIN framework allows dynamically updating the material state of the component and its individual locations. Hence, the MFIN framework presents opportunities to continually update material microstructural description from characterizations conducted at different stages of the product lifecycle, such as during the individual stages of manufacturing, acceptance of material from various vendors, and during periodic inspections of the component accounting for timedependent degradation or damage. By enabling the dynamic updating of data and seamless data exchange, the MFIN framework provides the use of precise microstructural descriptions within the subsequent microstructure-sensitive predictive analysis of a component, thereby further reducing uncertainties in the input microstructures and associated predicted life distributions. Additionally, we have demonstrated

the use of the as-designed or nominal component geometry within the lifing analysis. However, the MFIN framework can be potentially used for informing precise as-built geometries of individual components within lifing analysis (as shown in Fig. 2). Hence, the MFIN framework presents opportunities to create the digital twin of a serialized component to assist in decision-making during the product lifecycle.

The use of the MFIN framework for fatigue life assessment of components via physics-based simulations provides new opportunities to design the component and tailor the microstructure simultaneously, thus aiding in understanding the fatigue tradeoffs upfront during the product design stage. The framework can be extended by developing new MFIN schemas and wrapper code(s) to link to process modeling-related code(s) for predicting residual stress distributions, precipitates, grain sizes, texture evolution as well as property code(s) to compute strength by using structure–property linkages. By assessing current design strategies and understanding location-specific minimum life, engineers can potentially employ a fully model-based approach to iteratively redesign by modifying the geometry and/or the processing route to alter site-specific microstructures to optimize location-specific performance.

7. Conclusion

In this paper, a paradigm shift in the component analysis is enabled by developing a framework for microstructure-sensitive, location-specific lifing of components. The framework, namely the model-based feature information network (MFIN), enables tracking and retrieval of processing-induced microstructural information and stress/strain states resulting from in-service loading conditions at distinct locations in the component for use within a crystal plasticity fatigue life prediction model. A use case for lifing a dual microstructure heat treated (DMHT) LSHR turbine disk component is demonstrated at two locations, near the bore (fine grains) and near the rim (coarse grains) regions. From this framework, the contribution of this work is threefold:

- 1) Identifying material allowable life by utilizing location-specific microstructural knowledge in the component:
 - We demonstrated reduced uncertainties in the fatigue life distributions of LSHR in the DMHT turbine disk component and the associated minimum life (B0.1 life) by treating datasets corresponding to individual locations as separate distributions, which was enabled by the MFIN framework. The fatigue life predictions were obtained via crystal-plasticity finite element (CPFE) analysis, using statistically equivalent microstructures (SEMs) of the material, which were simulated under uniaxial loading conditions, akin to fatigue testing using virtual specimens. This approach presents opportunities to improve precision while determining the allowable minimum life by accounting for underlying microstructures at distinct locations in the component as opposed to the conventional approach of treating the entire component as a single monolithic structure with uniform microstructure.
 - The use of the microstructure-sensitive predictive analysis demonstrated in this study also presents opportunities to (i) reduce the overall number of tests needed to identify the minimum life, (ii) better understand the process-structure-property-performance relationship in the material by simulating multiple SEMs, and (iii) reduce time and costs associated with material testing during the product development stages.
- 2) A physics-based approach to assess the fatigue life of components:
 - A significant advancement in the present work is the extension of CPFE simulations to inform component scale life predictions. The principal strains from locations of interest in the component, calculated from component-level FE analysis, were precisely retrieved and used via the MFIN framework to inform multiaxial displacement boundary conditions in the sub-scale CPFE analysis.

- The location-specific fatigue life predictions facilitate opportunities to determine the critical or life-limiting locations of components with gradient microstructures.
- The framework and the lifing approach presented in this work provide new opportunities to design the component and tailoring site-specific microstructures simultaneously, thereby evaluating the fatigue tradeoffs upfront during the product design stage. By identifying the location corresponding to minimum life, one could potentially explore revisions to the design of the component geometry and/or the site-specific microstructure for optimizing the performance of the overall component.
- The hierarchical modeling approach does not rely on performing CPFE simulations for the entire component, thus providing judicious use of computational resources. Based on the combination of the component geometry, applied loading state, process and microstructure information, as well as legacy records tied to prior versions of the component, lifting engineers can down select the critical locations of components and use the proposed framework to perform higher fidelity CPFE simulations. Additionally, the framework inherently addresses the microstructural variability via simulating multiple SEMs, avoiding microstructure homogenization approaches, thus accounting for extreme values of the microstructural attributes while lifting components.
- Opportunities for performance analysis of components by utilizing a digital twin approach:
 - The MFIN framework facilitates storing, tracking, updating, and utilizing material microstructural definitions for fatigue life assessment. The use of data linkages in the MFIN framework creates dynamic connectivity to the current material state information in the component, which can be retrieved and used for future predictions of the component's performance with improved precision. Hence, by using the MFIN framework, we can continuously update the manufacturing process history, component geometry, material state information, and the associated stress distributions in each serialized component throughout the product lifecycle, thereby enabling a digital twin approach to assess the performance of individual components.
 - The MFIN framework is expandable to enable a fully model-based approach for assessing components. By creating necessary MFIN schemas and wrapper code(s), we can integrate process models and associated code(s), including the predictions of residual stress fields, grain size distributions, precipitate distributions, porosities, inclusions, surface features, in order to use the information effectively in subsequent performance analyses of components.

Declaration of Competing Interest

The authors declare that they have no known competing financial interests or personal relationships that could have appeared to influence the work reported in this paper.

Data availability

Data will be made available on request.

Acknowledgments

Funding has been provided by National Science Foundation under CMMI 16-51956. The authors would also like to thank Timothy Gabb and Ignacy Telesman from NASA GRC for providing the uniaxial tensile test data for LSHR, which were used in this work for crystal plasticity model calibration. We want to thank Dr. Nathan Hartman from Purdue University for collaboration on the model-based feature information network framework and Aidan Molnar from Purdue University for assistance with integrating the framework with a finite-element analysis tool and development of MFIN XML schemas for capturing crystal

plasticity information. Lastly, we would like to thank Daniel Campbell

from Capvidia for extending the MBDVidia license used in this study.

Appendix

Estimating initial CP model parameters via a macroscopic optimization scheme using the Kocks-Mecking formulation

To obtain initial estimates for the CP model parameters, initial reference stress (g(0)), initial dislocation density (ρ (0)), constant corresponding to dislocation storage (k_1), and constant corresponding to dislocation annihilation (k_2), we adapted the formulation proposed in [38] and conducted an optimization process to calibrate these parameters based on the macroscopic stress–strain data. This approach aids in selecting reasonable model parameter values as starting points, which can be subsequently refined to calibrate the final CP model parameters (Table 1). Additionally, the presented optimization scheme is computationally less intensive compared to running the CP model and allows us to run multiple iterations for selecting reasonable initial estimates of the fine and coarse grain model parameters.

Let us consider the evolution of total dislocation density (ρ) with incremental plastic strain (ϵ_{pl}) via a Kocks-Mecking type expression [38], described using k_1 and k_2 .

$$\frac{d\rho}{d\varepsilon_{pl}} = k_1 \sqrt{\rho} - k_2 \rho \tag{21}$$

Upon integrating Eq. (21), we can obtain an analytical expression of the dislocation density (ρ) as a function of plastic strain (ϵ_{pl}), and the terms k_1 and k_2 as shown in Eq. (22). Note that the integration constant was obtained by substituting $\rho = \rho(0)$, while using $\epsilon_{pl} = 0$.

$$\rho(\varepsilon_{pl}, k_1, k_2, \rho(0)) = \frac{\exp(-k_2 \varepsilon_{pl}) \left(\sqrt{(k_1 - k_2 \sqrt{\rho(0)})^2 - k_1 \exp(\frac{k_2 \varepsilon_{pl}}{2})}\right)^2}{k_2^2}$$
(22)

Next, we substitute the expression $\rho(\epsilon_{pl}, k_1, k_2, \rho(0))$ within the Taylor hardening description as shown in Eq. (23). The macroscopic flow stress evaluated using Eq. (23) is denoted as σ_{model} . The constant term α_1 is referred to as the interaction constant, which is typically of the order of unity and is dependent on the strength of dislocation–dislocation interactions [40]. The term σ_0 represents initial resistance to yielding and μ is the shear modulus.

$$\sigma_{\text{model}} = \sigma_0 + \alpha_1 \mu b \sqrt{\rho(\varepsilon_{\text{pl}}, k_1, k_2, \rho(0))}$$
(23)

To determine the unknowns σ_0 , $\rho(0)$, k_1 , and k_2 we set up an optimization scheme. We use the stress–strain data obtained from uniaxial tension tests (shown in Fig. 12(a)) for this purpose. The objective is to minimize the error, $f(\epsilon_{pl}, k_1, k_2, \rho(0))$, between σ_{model} from Eq. (23) and the stress (σ_{exp}) from the uniaxial tension tests, as shown in Eq. (24).

$$Minimize: f(\varepsilon_{pl}, k_1, k_2, \rho(0)) = \| \sigma_{exp} - \sigma_{model} \|_2$$

$$(24)$$

For solving the optimization problem described in Eq. (24), the initial guesses for the unknown parameters were chosen as follows. The values of macroscopic yield stress were used as initial guesses for σ_0 . For fine grain microstructure, an initial guess of $\sigma_0=1209$ MPa was used, whereas for the coarse grain microstructure, an initial guess of $\sigma_0=1074$ MPa was used. In Ni-based superalloys, we typically expect $\rho(0)$ on the order of 10^5-10^6 ($\frac{1}{mm^2}$). For both the fine grain and coarse grain microstructures, we assume a starting value of 10^6 ($\frac{1}{mm^2}$) in this analysis. Based on [38], a reasonable initial estimate for k_1 is $1/100\alpha_1 b$, where the Burger vector (b) is 2.54 Å. Since, α_1 typically ranges between 0.1 and 1 [40], we assumed a constant value of $\alpha_1=0.3$. Finally, from previous works [14,56], the value of k_2 is on the order of 10; hence, we assume a starting value of $k_2=10$, for both the microstructures. For accommodating a broader search space, random perturbations were applied to the initial guesses, and 1000 optimization iterations were repeated.

Finally, using the optimization routine, we obtained the following estimates for the unknown quantities σ_0 , $\rho(0)$, k_1 , and k_2 that minimized the error function $f(\epsilon_{pl},k_1,k_2,\rho(0))$. For the fine grain microstructure, we determined $\sigma_0=1183$ MPa, $\rho(0)=10^6\frac{1}{mm^2}$, $k_1=2.85$ X $10^6\frac{1}{mm}$, and $k_2=30.38$. For the coarse grain microstructure, the values of $\sigma_0=1120$ MPa, $\rho(0)=10^6\frac{1}{mm^2}$, $k_1=1.68$ X $10^6\frac{1}{mm}$, and $k_2=19.77$ were identified. We observe that the values of k_1 and k_2 for the fine grain microstructure is greater than the values obtained for the coarse grain microstructure. Since the LSHR material displays random texture, the initial resistance at the slip system level for the CP model parameter g(0) is obtained from σ_0 by dividing with the Taylor factor for uniaxial loading with random texture, 3.06. Hence, we obtain an initial estimate of g(0)=387 MPa for the fine grain microstructure and g(0)=366 MPa for the coarse grain microstructure.

Additionally, the constant parameters Γ_{act} , D, h_n in the expression which relates k_1 and k_2 (Eq. (7)) were selected. The term h_n is related to the interaction constant α_1 , i.e., $h_n = \alpha_1^2$, such that $h_n = 0.09$ for the present work. For identifying Γ_{act} and D, we use the values of $\frac{k_2}{k_1}$ for both the fine grain and coarse grain microstructures and substitute the values within Eq. (7). We obtained $\frac{k_2}{k_1} = 1.12X10^{-5}$ for the fine grain microstructure and $\frac{k_2}{k_1} = 1.06X10^{-5}$ for the coarse grain microstructure. From these ratios, a combination of values for $\Gamma_{act} = 2.88 \times 10^{-3}$ and D = 53280 MPa were determined for both microstructures using Eq. (7). It is worth noting that $\frac{k_2}{k_1}$ from our initial estimates were approximately equal in magnitude. This is further supported by Fig. 12(b). By using the experimental dataset and plotting the $(d\sigma/d\epsilon)/E$ (wherein E is the Young's modulus) versus σ/σ_{YS} (wherein σ_{YS} is the yield stress) for both the microstructures, we can observe that the hardening curves of both materials become equivalent, as pointed out in Fig. 12(b). Lastly, as seen in Fig. 12(a), the stress–strain curves for the fine and coarse grain materials reveal a discrepancy in the elastic modulus for these materials. The preferred measure of elastic moduli values are not identified from ASTM E21 tensile experiments, and no other information was available. The single crystal elastic constants for constant composition, fine and coarse grain material are expected to be consistent, yet differences in the precipitate structure can influence these values. For this work, the elastic constants were scaled from values reported in [42] during calibration to provide agreement with the available data. For future work, additional experimental test data is recommended to identify the elastic modulus across the component and determine the appropriate set of single crystal elastic constants for both the fine and coarse grain material.

References

- [1] National Research Council. Integrated computational materials engineering: a transformational discipline for improved competitiveness and national security. National Academies Press; 2008.
- [2] Gabb TP, Kantzos PT, Telesman J, Gayda J, Sudbrack CK, Palsa B. Fatigue resistance of the grain size transition zone in a dual microstructure superalloy disk. Int J Fatigue 2011;33:414–26. https://doi.org/10.1016/j.ijfatigue.2010.09.022.
- [3] Gayda J, Gabb TP, Kantzos PT. The effect of dual microstructure heat treatment on an advanced nickel-base disk alloy. Proceedings of the International Symposium on Superalloys 2004:323–9. https://doi.org/10.7449/2004/superalloys_2004_323_ 329
- [4] Mitchell RJ, Lemsky JA, Ramanathan R, Li HY, Perkins KM, Connor LD. Process development & microstructure & mechanical property evaluation of a dual microstructure heat treated advanced nickel disc alloy. Proceedings of the International Symposium on Superalloys 2008:347–56. https://doi.org/10.7449/ 2008/superalloys 2008 347 356.
- [5] Furrer DU, Dimiduk DM, Cotton JD, Ward CH. Making the Case for a Model-Based Definition of Engineering Materials. Integrating Materials and Manufacturing Innovation 2017;6:249–63. https://doi.org/10.1007/s40192-017-0102-7.
 [6] Larsen JM, Jha SK, Szczepanski CJ, Caton MJ, John R, Rosenberger AH, et al.
- [6] Larsen JM, Jha SK, Szczepanski CJ, Caton MJ, John R, Rosenberger AH, et al. Reducing uncertainty in fatigue life limits of turbine engine alloys. Int J Fatigue 2013;57:103–12. https://doi.org/10.1016/j.ijfatigue.2013.01.012.
- [7] Christodoulou L, Larsen JM. Using materials prognosis to maximize the utilization potential of complex mechanical systems. JOM 2004;56:15–9. https://doi.org/ 10.1007/s11837-004-0027-4.
- [8] Furrer DU, Shankar R, White C. Optimizing the heat treatment of Ni-based superalloy turbine discs. Jom 2003;55:32–4. https://doi.org/10.1007/s11837-003-0157-0.
- [9] McDowell DL, Dunne FPE. Microstructure-sensitive computational modeling of fatigue crack formation. Int J Fatigue 2010;32:1521–42. https://doi.org/10.1016/ i.iifatigue.2010.01.003.
- [10] Anahid M, Samal MK, Ghosh S. Dwell fatigue crack nucleation model based on crystal plasticity finite element simulations of polycrystalline titanium alloys. J Mech Phys Solids 2011;59:2157–76. https://doi.org/10.1016/j. jmps.2011.05.003.
- [11] Wan VVC, Maclachlan DW, Dunne FPE. A stored energy criterion for fatigue crack nucleation in polycrystals. Int J Fatigue 2014;68:90–102. https://doi.org/ 10.1016/j.jifatigue.2014.06.001.
- [12] Chen B, Jiang J, Dunne FPE. Is stored energy density the primary meso-scale mechanistic driver for fatigue crack nucleation? Int J Plast 2018;101:213–29. https://doi.org/10.1016/j.ijplas.2017.11.005.
- [13] Bandyopadhyay R, Prithivirajan V, Peralta AD, Sangid MD. Microstructuresensitive critical plastic strain energy density criterion for fatigue life prediction across various loading regimes. Proceedings of the Royal Society A: Mathematical, Physical and Engineering Sciences 2020;476. https://doi.org/10.1098/ rspa.2019.0766.
- [14] Bandyopadhyay R, Sangid MD. A Probabilistic Fatigue Framework to Enable Location - Specific Lifing for Critical Thermo - mechanical Engineering Applications. Integrating Materials and Manufacturing Innovation 2021. https://doi.org/10.1007/s40192-021-00198-4.
- [15] Prithivirajan V, Sangid MD. Examining metrics for fatigue life predictions of additively manufactured IN718 via crystal plasticity modeling including the role of simulation volume and microstructural constraints. Mater Sci Eng, A 2020;783: 139312. https://doi.org/10.1016/j.msea.2020.139312.
- [16] Tuegel EJ, Ingraffea AR, Eason TG, Spottswood SM. Reengineering aircraft structural life prediction using a digital twin. International Journal of Aerospace Engineering 2011;2011. https://doi.org/10.1155/2011/154798.
- [17] Glaessgen E, Stargel D. The Digital Twin Paradigm for Future NASA and U.S. Air Force Vehicles. 53rd AIAA/ASME/ASCE/AHS/ASC Structures, Structural Dynamics and Materials Conference
20th AIAA/ASME/AHS Adaptive Structures Conferece
14th AIAA 2012:1–14. https://doi.org/10.2514/ 6.2012-1818.
- [18] AIAA Digital Engineering Integration Committee. Digital Twin: Definition & Value. An AIAA and AIA Position Paper 2020:1–16.
- [19] Gopalakrishnan S, Hartman NW, Sangid MD. Model-Based Feature Information Network (MFIN): A Digital Twin Framework to Integrate Location-Specific Material Behavior Within Component Design, Manufacturing, and Performance Analysis. Integrating Materials and Manufacturing Innovation 2020;9:394–409. https://doi.org/10.1007/s40192-020-00190-4.
- [20] Astheimer R, Del RK, Gopalakrishnan S, Hartman N, Sangid M. Extending Model Based Definition to Capture Product Behavior and Contextual Information using a Model Based Feature Information. Network 2019:253–7. https://doi.org/10.1 4733/cadconfp.2019.253-257.
- [21] ISO 23952:2020 Automation systems and integration Quality information framework (QIF) — An integrated model for manufacturing quality information. 1st ed. International Organization of Standardization (https://www.iso.org/ standard/77461.html); 2020.
- [22] MBDVidia 4.0 Software (Capvidia) n.d. https://www.capvidia.com/products/mbdvidia [Accessed date: October 2020].
- [23] Siemens NX 12.0 CAD Documentation n.d. https://docs.plm.automation.siemens. com/tdoc/nx/12/nx_help/#uid:index [Accessed date: October 2020].
- [24] Bigot PA. PyXB: Python XML Schema Bindings 2014. http://pyxb.sourceforge.net/. [Accessed date: October 2020].
- [25] Leach P, Mealling M, Salz R. RFC 4122: A universally unique identifier (UUID) URN namespace. (Https://WwwletfOrg/Rfc/Rfc4122Txt) 2005.

- [26] Granta Design n.d. https://www.grantadesign.com/industry/products/granta-mi/ [Accessed date: April 2nd 2020].
- [27] MSC. Material Center 2016. https://www.mscsoftware.com/product/materialcenter (accessed November 16, 2020).
- [28] Gopalakrishnan S, Hartman NW, Sangid MD. A digital engineering framework to facilitate automated data exchange between geometric inspection and structural analysis. (under review) 2022.
- [29] ISO 10303-214, 2010. Industrial automation systems and integration Product data representation and exchange – Part 214: Application protocol: Core data for automotive mechanical design process. International 2010.
- [30] Gabb TP, Kantzos PT, Palsa B, Telesman J, Gayda J, Sudbrack CK. Fatigue Failure Modes of the Grain Size Transition Zone in a Dual Microstructure Disk. Superalloys 2012;2012:63–72. https://doi.org/10.1002/9781118516430.ch7.
- [31] Gayda J, Furrer D. Dual microstructure heat treatment. Adv Mater Processes 2003;
- [32] Gabb TP, Gayda J, Telesman J, Kantzos PT. Thermal and Mechanical Property Characterization of the Advanced Disk Alloy LSHR - Technical Memorandum 2005: 82.
- [33] Collins DM, Stone HJ. A modelling approach to yield strength optimisation in a nickel-base superalloy. Int J Plast 2014;54:96–112. https://doi.org/10.1016/j. ijplas.2013.08.009.
- [34] Groeber MA, Jackson MA. DREAM.3D: A Digital Representation Environment for the Analysis of Microstructure in 3D 2014;3:5.
- [35] Bandyopadhyay R, Prithivirajan V, Sangid MD. Uncertainty Quantification in the Mechanical Response of Crystal Plasticity Simulations. Jom 2019;71:2612–24. https://doi.org/10.1007/s11837-019-03551-3.
- [36] Prithivirajan V, Sangid MD. The role of defects and critical pore size analysis in the fatigue response of additively manufactured IN718 via crystal plasticity. Mater Des 2018;150:139–53. https://doi.org/10.1016/j.matdes.2018.04.022.
- [37] Physics A. Bounds and self-consistent estimates for creep of polycrystalline materials. Proceedings of the Royal Society of London A Mathematical and Physical Sciences 1976;348:101–27. https://doi.org/10.1098/rspa.1976.0027.
- [38] Mecking H, Kocks UF. Kinetics of flow and strain-hardening. Acta Metall 1981;29: 1865–75. https://doi.org/10.1016/0001-6160(81)90112-7.
- [39] Kocks UF, Mecking H. Physics and phenomenology of strain hardening: The FCC case. Prog Mater Sci 2003;48:171–273. https://doi.org/10.1016/S0079-6425(02) 00003-8.
- [40] Beyerlein IJ, Tomé CN. A dislocation-based constitutive law for pure Zr including temperature effects. Int J Plast 2008;24:867–95. https://doi.org/10.1016/j. iiplas.2007.07.017.
- [41] Cheng J, Shahba A, Ghosh S. Stabilized tetrahedral elements for crystal plasticity finite element analysis overcoming volumetric locking. Comput Mech 2016;57: 733–53. https://doi.org/10.1007/s00466-016-1258-2.
- [42] Boyce D, Shade P, Musinski W, Obstalecki M, Pagan D, Bernier J, et al. Estimation of anisotropic elastic moduli from high energy X-Ray data and finite element simulations. Materialia 2020;12:100795. https://doi.org/10.1016/j. mtla.2020.100795.
- [43] Morrow J. Cyclic plastic strain energy and fatigue of metals. In: Lazan B, editor. Internal friction, damping, and cyclic plasticity. West Conshohocken, PA: ASTM International; 1965. p. 45–87.
- [44] Prithivirajan V, Ravi P, Naragani D, Sangid MD. Direct comparison of microstructure-sensitive fatigue crack initiation via crystal plasticity simulations and in situ high-energy X-ray experiments. Mater Des 2021;197:109216. https:// doi.org/10.1016/j.matdes.2020.109216.
- [45] Nicolas A, Co NEC, Burns JT, Sangid MD. Predicting fatigue crack initiation from coupled microstructure and corrosion morphology effects. Eng Fract Mech 2019; 220:106661. https://doi.org/10.1016/j.engfracmech.2019.106661.
- [46] Sangid MD, Maier HJ, Sehitoglu H. An energy-based microstructure model to account for fatigue scatter in polycrystals. J Mech Phys Solids 2011;59:595–609. https://doi.org/10.1016/j.jmps.2010.12.014.
- [47] Thompson AW, Backofen WA. The effect of grain size on fatigue. Acta Metall 1971; 19:597–606. https://doi.org/10.1016/0001-6160(71)90012-5.
- [48] Thompson AW. The comparison of yield and fatigue strength dependence on grain size. Scr Metall 1971;5:859–63. https://doi.org/10.1016/0036-9748(71)90059-7.
- [49] Morrison DJ, Moosbrugger JC. Effects of grain size on cyclic plasticity and fatigue crack initiation in nickel. Int J Fatigue 1997;19. https://doi.org/10.1016/s0142-1123(97)00034-0.
- [50] Sangid MD, Maier HJ, Sehitoglu H. A physically based fatigue model for prediction of crack initiation from persistent slip bands in polycrystals. Acta Mater 2011;59: 328–41. https://doi.org/10.1016/j.actamat.2010.09.036.
- [51] Johnson GRCWH. A constitutive model and data for metals.pdf. In: Proceedings of the Seventh International Symposium; 1983. p. 541–7.
- [52] Kobryn P, Tuegel E, Zweber J, Kolonay R. Digital thread and twin for systems engineering: EMD To disposal. AIAA SciTech Forum - 55th AIAA Aerospace Sciences Meeting 2017:1–13. https://doi.org/10.2514/6.2017-0876.
- [53] James LA. The effect of grain size upon the fatigue-crack propagation behavior of alloy 718 under hold-time cycling at elevated temperature. Eng Fract Mech 1986; 25:305–14. https://doi.org/10.1016/0013-7944(86)90127-X.
- [54] Gopalakrishnan S, Hartman NW, Sangid MD. Integrating materials model-based definitions into design, manufacturing, and sustainment: a digital twin demonstration of incorporating residual stresses in the lifecycle analysis of a

- turbine disk. J Comput Inf Sci Eng 2020;21:1–25. https://doi.org/10.1115/
- [55] Acharya A, Beaudoin AJ. Grain-size effect in viscoplastic polycrystals at moderate strains. J Mech Phys Solids 2000;48:2213–30. https://doi.org/10.1016/S0022-5096(00)00013-2.
- [56] Bandyopadhyay R, Sangid MD. Crystal plasticity assessment of inclusion- and matrix-driven competing failure modes in a nickel-base superalloy. Acta Mater 2019;177:20–34. https://doi.org/10.1016/j.actamat.2019.07.024.